



**NAVAL  
POSTGRADUATE  
SCHOOL**

**MONTEREY, CALIFORNIA**

**THESIS**

**AN INVERSE MODEL OF DOUBLE DIFFUSIVE  
CONVECTION IN THE BEAUFORT SEA**

by

Jeremiah E. Chaplin

December 2009

Thesis Advisor:

Timour Radko

Second Reader:

Arthur Schoenstadt

**Approved for public release; distribution is unlimited**

<b>REPORT DOCUMENTATION PAGE</b>		Form Approved OMB No. 0704-0188	
Public reporting burden for this collection of information is estimated to average 1 hour per response, including the time for reviewing instruction, searching existing data sources, gathering and maintaining the data needed, and completing and reviewing the collection of information. Send comments regarding this burden estimate or any other aspect of this collection of information, including suggestions for reducing this burden, to Washington headquarters Services, Directorate for Information Operations and Reports, 1215 Jefferson Davis Highway, Suite 1204, Arlington, VA 22202-4302, and to the Office of Management and Budget, Paperwork Reduction Project (0704-0188) Washington DC 20503.			
<b>1. AGENCY USE ONLY (Leave blank)</b>		<b>2. REPORT DATE</b> December 2009	<b>3. REPORT TYPE AND DATES COVERED</b> Master's Thesis
<b>4. TITLE AND SUBTITLE</b> An Inverse Model of Double Diffusive Convection in the Beaufort Sea		<b>5. FUNDING NUMBERS</b>	
<b>6. AUTHOR(S)</b> Jeremiah E. Chaplin		<b>8. PERFORMING ORGANIZATION REPORT NUMBER</b>	
<b>7. PERFORMING ORGANIZATION NAME(S) AND ADDRESS(ES)</b> Naval Postgraduate School Monterey, CA 93943-5000		<b>10. SPONSORING/MONITORING AGENCY REPORT NUMBER</b>	
<b>9. SPONSORING /MONITORING AGENCY NAME(S) AND ADDRESS(ES)</b> N/A		<b>11. SUPPLEMENTARY NOTES</b> The views expressed in this thesis are those of the author and do not reflect the official policy or position of the Department of Defense or the U.S. Government.	
<b>12a. DISTRIBUTION / AVAILABILITY STATEMENT</b> Approved for public release; distribution is unlimited		<b>12b. DISTRIBUTION CODE</b>	
<b>13. ABSTRACT (maximum 200 words)</b> This study explores the fluxes of heat and salt associated with thermohaline staircases in the Beaufort Sea. An inverse model is developed to calculate the vertical transport of properties in the southern portion of the Beaufort Sea directly from observations. The applicability of laboratory derived 4/3 flux law is addressed. Three formulations of the static advective-diffusive equations are discretized on a uniform grid, and inverted using the method of Total Least Squares. The first formulation is based on the classic flux-gradient model, and is analyzed in both one and three-dimensions. The second formulation utilizes Turner formulation of the 4/3 flux law, but the formulation of the coefficient $C(R_p)$ remains unknown. The third formulation includes the full form of the Kelley model, but the amplitude of $C(R_p)$ is unknown. Layer averaged heat flux through the thermohaline staircases is found to be on the order of $1 \text{ W/m}^2$ , which is significantly higher than previous studies. This implies that the laboratory formulation of the 4/3 flux law may require calibration in order to accurately represent Arctic conditions.			
<b>14. SUBJECT TERMS</b> Double Diffusion, Inverse Model, 4/3 Flux Law		<b>15. NUMBER OF PAGES</b> 89	
		<b>16. PRICE CODE</b>	
<b>17. SECURITY CLASSIFICATION OF REPORT</b> Unclassified	<b>18. SECURITY CLASSIFICATION OF THIS PAGE</b> Unclassified	<b>19. SECURITY CLASSIFICATION OF ABSTRACT</b> Unclassified	<b>20. LIMITATION OF ABSTRACT</b> UU

THIS PAGE INTENTIONALLY LEFT BLANK

Approved for public release; distribution is unlimited

**AN INVERSE MODEL OF DOUBLE DIFFUSIVE CONVECTION IN THE  
BEAUFORT SEA**

Jeremiah E. Chaplin  
Lieutenant, United States Navy  
B.A., San Diego State University, 2002

Submitted in partial fulfillment of the  
requirements for the degree of

**MASTER OF SCIENCE IN  
METEOROLOGY AND PHYSICAL OCEANOGRAPHY**

from the

**NAVAL POSTGRADUATE SCHOOL  
December 2009**

Author: Jeremiah E. Chaplin

Approved by: Timour Radko  
Thesis Advisor

Arthur Schoenstadt  
Second Reader

Jeffrey Paduan  
Chairman, Department of Oceanography

THIS PAGE INTENTIONALLY LEFT BLANK

## ABSTRACT

This study explores the fluxes of heat and salt associated with thermohaline staircases in the Beaufort Sea. An inverse model is developed to calculate the vertical transport of properties in the southern portion of the Beaufort Sea directly from observations. The applicability of laboratory derived  $4/3$  flux law is addressed. Three formulations of the static advective-diffusive equations are discretized on a uniform grid, and inverted using the method of Total Least Squares. The first formulation is based on the classic flux-gradient model, and is analyzed in both one and three-dimensions. The second formulation utilizes Turner formulation of the  $4/3$  flux law, but the formulation of the coefficient  $C(R_\rho)$  remains unknown. The third formulation includes the full form of the Kelley model, but the amplitude of  $C(R_\rho)$  is unknown. Layer averaged heat flux through the thermohaline staircases is found to be on the order of  $1 \text{ W/m}^2$ , which is significantly higher than previous studies. This implies that the laboratory formulation of the  $4/3$  flux law may require calibration in order to accurately represent Arctic conditions.

THIS PAGE INTENTIONALLY LEFT BLANK

## TABLE OF CONTENTS

I.	INTRODUCTION AND BACKGROUND .....	1
A.	ARCTIC CIRCULATION .....	1
B.	DOUBLE-DIFFUSIVE CONVECTION .....	2
C.	EARLIER ESTIMATES OF HEAT FLUX .....	6
D.	INVERSE MODELING .....	10
E.	UNRESOLVED ISSUES .....	11
II.	DATA AND DATA PROCESSING .....	13
A.	ICE-TETHERED PROFILER DATA .....	13
B.	DATA PROCESSING .....	16
C.	INTERPOLATING DATA TO A GRID .....	21
III.	INVERSE MODEL .....	25
A.	MODEL FRAMEWORK .....	25
B.	THE "BEST" SOLUTION TO THE OVERDETERMINED SYSTEM ..	30
C.	SCALING THE MATRIX .....	36
D.	PARAMETERIZATIONS OF THE VERTICAL FLUXES .....	37
IV.	MODEL RESULTS .....	39
A.	ONE-DIMENSIONAL MODEL .....	39
B.	THREE-DIMENSIONAL MODEL .....	45
1.	Depth Dependent Discretization .....	45
2.	4/3 Flux Law Discretization with $C(R_p)$ Unknown .....	50
3.	$C(R_p)$ Calculation using Kelley (1990) 4/3 Flux Law .....	54
V.	DISCUSSION AND CONCLUSIONS .....	61
A.	DISCUSSION .....	61
B.	CONCLUSIONS .....	65
C.	RECOMMENDATIONS .....	66
	LIST OF REFERENCES .....	69
	INITIAL DISTRIBUTION LIST .....	73



THIS PAGE INTENTIONALLY LEFT BLANK

## LIST OF FIGURES

Figure 1.	The oscillatory regime of double diffusive convection.....	3
Figure 2.	Temperature - Salinity (From Timmermans, 2008)...	4
Figure 3.	Diffusive Layering - Fluxes of heat and salt are transported upward across the thin layer, causing convection and mixing within the homogeneous layers.....	5
Figure 4.	Ice tethered profiler system.....	14
Figure 5.	Location of ITP 1-6.....	15
Figure 6.	Temperature - Salinity plot for ITPs 1-6.....	18
Figure 7.	Histogram of data: Number of data points for a given salinity value.....	19
Figure 8.	Locations of each profile.....	21
Figure 9.	Location of the three-dimensional dataset.....	22
Figure 10.	(a) Salinity surfaces for 19 layers used in the inverse calculation. (b) The corresponding potential Temperature surfaces.....	23
Figure 11.	The seven-point grid network for finite differencing. (After Lee & Veronis, 1991).....	26
Figure 12.	Least squares and total least squares fits of a set of $m=20$ data points in the plane and just one unknown $\mathbf{x}$ . $\mathbf{a}_i$ and $\mathbf{b}_i$ represent the components of an example data matrix $\mathbf{a}$ and an observation vector $\mathbf{b}$ . In the least squares fit the error only exists in $\mathbf{b}$ and in the total least squares fit errors exist in both $\mathbf{a}$ and $\mathbf{b}$ . (From Markovsky et al., 2007).....	30
Figure 13.	Least Squares and Total Least Squares fits of a plane $\mathbf{A}$ and vector $\mathbf{b}$ . The plane $\mathbf{A}$ is a representation of all possible values for $\mathbf{Ax}$ . Ultimately only one vector $\mathbf{Ax}$ represents the closest approximation of $\mathbf{b}$ . (a) LS minimizes the vector $-\mathbf{r}$ , where $-\mathbf{r}$ only represents error in the vector $\mathbf{b}$ , by projecting $\mathbf{b}$ onto the plane $\mathbf{A}$ . (b) TLS minimizes $-\mathbf{[E r]}$ which represents the error in both $\mathbf{A}$ and $\mathbf{b}$ , needed to project $\mathbf{b}$ onto the perturbed plane $\mathbf{A}$ . Both the data matrix and the observation vector are corrected to find an exact solution.....	31
Figure 14.	The importance of similar norms for $\mathbf{A}$ and $\mathbf{b}$ . (a) A properly scaled problem, where $\mathbf{A}$ and $\mathbf{b}$ have the same norm. (b) The norms of $\mathbf{A}$ and $\mathbf{b}$ differ by a factor of four.....	33

Figure 15.	Comparison of the two laboratory representations of Heat Flux and the calculated value of Heat Flux from the one-dimensional Model 1.....	42
Figure 16.	Fit of $C(R_p)$ as proposed by Kelley (1990) to the one dimensional Model 1 results.....	44
Figure 17.	Comparison of the two laboratory representations of Heat Flux and the calculated value of Heat Flux from the three-dimensional Model 1.....	47
Figure 18.	Fit of $C(R_p)$ as proposed by Kelley (1990) to the three dimensional model 1 results.....	49
Figure 19.	Comparison of the two laboratory representations of $C(R_p)$ and the calculated value of $C(R_p)$ from the three-dimensional Model 2.....	53
Figure 20.	Fit of $C(R_p)$ as proposed by Kelley (1990) to the three-dimensional Model 2 results.....	54
Figure 21.	Comparison of the two laboratory representations of $C(R_p)$ and the calculated value of $C(R_p)$ from the three-dimensional Model 3.....	58

## LIST OF TABLES

Table 1.	Number of Observations (individual data points) for Each Profile. Each profile has up to the maximum number of observations indicated. Not all profiles have the maximum number of observations.....	17
Table 2.	Number of Layers for Each Profile.....	17
Table 3.	Total number of layers and profiles in final data set.....	20
Table 4.	One dimensional data set consisting of average values of potential temperature, salinity, and layer thickness for the entire basin.....	40
Table 5.	One-dimensional Model 1 results.....	41
Table 6.	Comparison of heat flux calculated using the one dimensional Model 1 and using Kelley (1990) formulation of the 4/3 flux law.....	43
Table 7.	Three dimensional Model 1 results.....	46
Table 8.	Comparison of heat flux calculated using the three-dimensional Model 1 and the Kelley (1990) formulation of the 4/3 flux law.....	48
Table 9.	Three-dimensional Model 2 results.....	51
Table 10.	Comparison of heat flux calculated using the three-dimensional model 2 and the Kelley (1990) formulation of the 4/3 flux law.....	52
Table 11.	Three-dimensional Model 3 results.....	57
Table 12.	Comparison of heat flux calculated using the three-dimensional Model 3 and the Kelley (1990) formulation of the 4/3 flux law.....	57
Table 13.	Comparison of heat fluxes calculated from all models.....	61
Table 14.	Mean layer thicknesses.....	62
Table 15.	Comparison of amplitudes of the 4/3 flux law coefficient $C(R_\rho)$ .....	64

THIS PAGE INTENTIONALLY LEFT BLANK

## ACKNOWLEDGMENTS

I would first and foremost like to thank my family for enduring this entire process. Obtaining a master's level education is no small feat, and without the love and support of my entire family, I would not have had the fortitude to complete this work. Particular thanks must go to my wife and daughter for sacrificing critical family time for the benefit of this thesis, and my education as a whole. I love you both very much.

I would also like to thank Professor Radko for your patience while I learned the mathematics necessary to complete this thesis. Your confidence in my ability to learn the inverse modeling process was a huge factor in my success. You instilled a confidence in me that allowed me to focus on accomplishing our goals. Your expertise in the physics proved absolutely critical to obtaining meaningful results. I look forward to future work with you.

Finally, I have to thank Professor Schoenstadt for coming out of retirement and spending countless hours of your own time to ensure I had a good mathematical foundation to do what was required for this thesis. Your tutoring sessions were above and beyond anything I ever imagined when I asked for your help. Without you, this thesis simply wouldn't have happened.

Thank you all.

THIS PAGE INTENTIONALLY LEFT BLANK

## **I. INTRODUCTION AND BACKGROUND**

### **A. ARCTIC CIRCULATION**

Sea ice in the Arctic is melting at an alarming rate, much faster than expected (Stroeve et al., 2007). The years 2007-2009 have seen the lowest summer sea ice coverage in the Arctic in the modern era. Ice melt in the Arctic has been largely attributed to rising greenhouse gas concentrations and the associated warming of the atmosphere. The ocean, however, responds to the atmospheric conditions on much longer time scales. We are only beginning to understand the response of the Arctic Ocean to the atmospheric forcing associated with climate change (Stroeve & Maslowski, 2008; Dickson et al., 2000). One such response is the delivery of significantly elevated quantities of warmer water to the Canada Basin and Beaufort Sea. This additional warm water, which has taken decades to traverse the Canada Basin, adds significant amounts of heat to the upper Arctic Ocean, aggravating the ice melt problem.

The heat stored in the oceans directly influences the melting rate of the ice from below. Perovich et al. (2003) showed a 1-2 W/m<sup>2</sup> difference between the amount of heat necessary to melt the ice from below and the atmospheric heat fluxes calculated over open water. They suggest that there must be oceanic sources of heat to the ocean-ice interface. Understanding the mechanisms that drive the heat flux to the ice from the ocean is critical to the explanation and prediction of increased sea ice melt. The ocean can play a role in melting sea ice via several



mechanisms. Ice-ocean interactions include horizontal advection of warm water from the Pacific and Atlantic oceans under the ice cover; the accumulation of heat due to increased solar radiation in ice diminished regions; and locally induced upward heat flux into the mixed layer due to upwelling, topographically controlled flow, and eddies (Maslowski et al., 2009).

This thesis will focus on the role of double diffusion in oceanic heat transfer, which is a subject of growing interest in oceanography and Arctic sciences. It is argued that double-diffusive convection may also play a significant role in transferring heat upward into the Arctic mixed layer. The heat transported toward the ocean surface via diffusive convection may be a critical component to understanding the connection between ocean dynamics and sea ice extent in the Arctic.

## **B. DOUBLE-DIFFUSIVE CONVECTION**

Double diffusion is defined as a set of processes related to the difference in molecular diffusivities of heat and salt. It is known to influence vertical mixing in the ocean, and comes in two forms: salt fingering and diffusive convection. Salt fingering is prevalent in the mid-latitudes, while diffusive convection is the form of double diffusion seen in the Arctic.

The term diffusive convection is used to describe two types of motion that arise in fluids with a negative vertical gradient of temperature and salinity. The first is characterized by oscillations in smooth temperature-salinity gradients. The other, diffusive layering, operates in a

thin interface, which separates two homogeneous layers. Heat and salt are transferred across the diffusive interface.

The oscillatory regime of double diffusive convection is described in Figure 1.

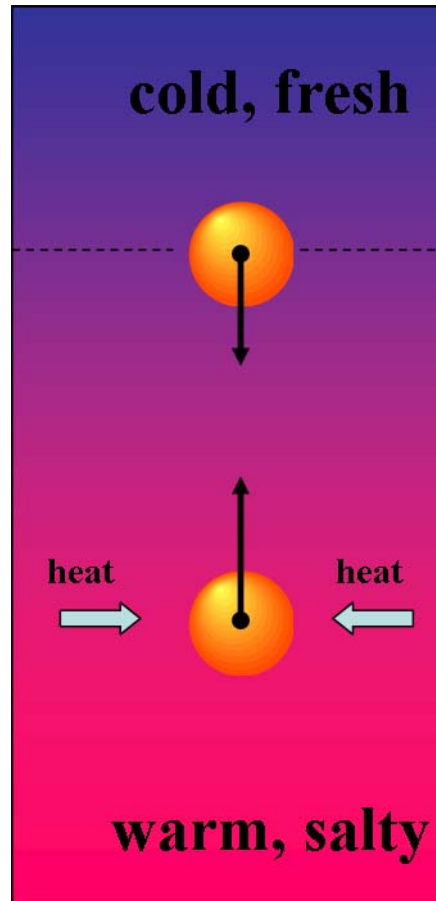


Figure 1. The oscillatory regime of double diffusive convection

Imagine a parcel of water in a lower layer that is displaced upward. This parcel is warmer and more saline than the layer of water above. As the parcel enters the layer above, it immediately begins to lose heat, via molecular diffusion, to the surrounding upper layer at a rate nearly 100 times as fast as it loses salt. The result is cooling of the parcel, while it maintains its salinity.

The parcel then begins to descend, due to its increasing density, as it cools. The denser parcel begins to gain heat in the lower, warmer layer, again via molecular diffusion, and once it gains a sufficient amount of heat its density decreases and the parcel begins to rise again. This mixing results in the formation of layers of near constant temperature and salinity. It is these layers that define the second form of diffusive convection, diffusive layering. This process is known to be prevalent in the Beaufort Sea.

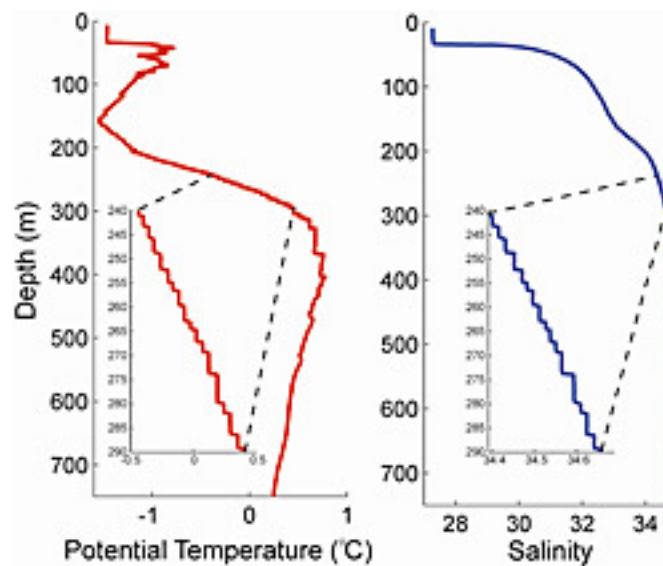


Figure 2. Temperature - Salinity (From Timmermans, 2008)

Diffusive layering occurs in a stable environment, where, in the case of the Arctic, cold fresh water overlies warm and salty water, as seen in Figure 2.

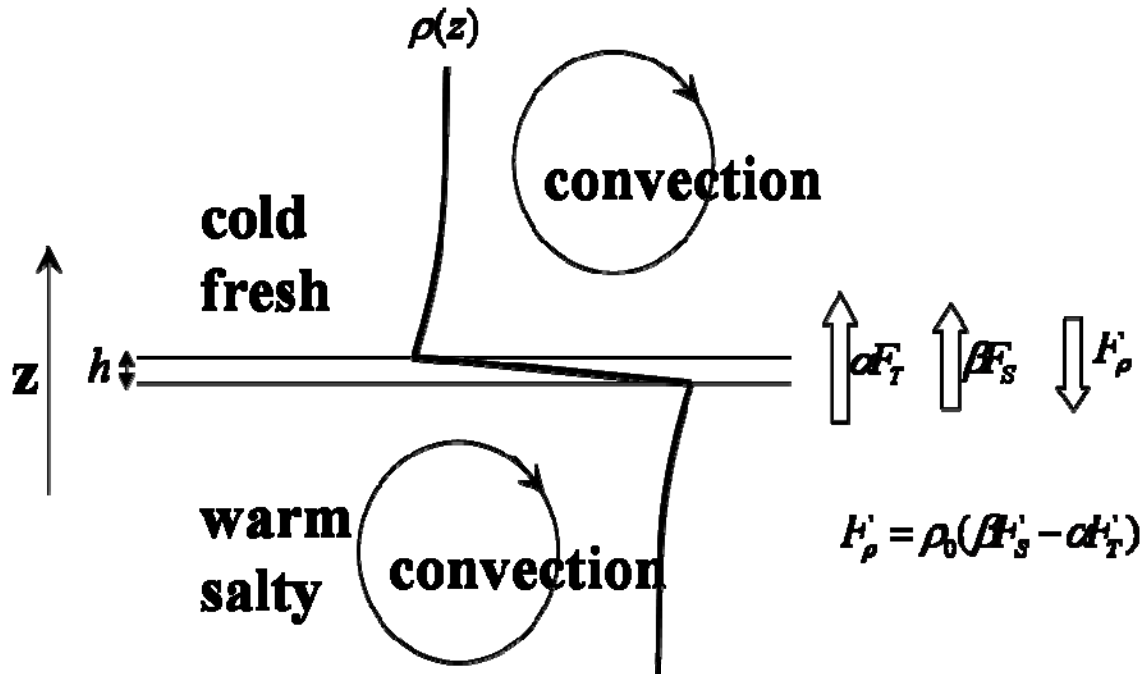


Figure 3. Diffusive Layering - Fluxes of heat and salt are transported upward across the thin layer, causing convection and mixing within the homogeneous layers.

Diffusive layering is manifested in the Arctic thermocline by a series of homogeneous layers of near constant temperature and salinity separated by a thin diffusive interface. This natural occurrence is often referred to as a thermohaline staircase. The physical processes associated with the maintenance of this structure (Figure 3) can be described as follows: Heat and salt are transferred upward through the diffusive interface. The water just above the interface gains sufficient heat to begin upward motion due to excess of buoyancy. This water begins to rise within the layer, driving the convection that ultimately maintains the homogeneous properties of the mixed layer.

The data shown in Figure 2 are representative of the majority of the data collected by the Woods Hole Oceanographic Institute (WHOI) Ice Tethered Profiler (ITP) program. The warm water seen from ~300 meters and below originates in the Pacific and Atlantic oceans and is advected into the Beaufort Sea via the Arctic current system. The cold water above is a result of downward temperature flux associated with the cold surface and air-sea-ice interaction. The less saline, or relatively fresh, surface water is a result of annual ice melt and fresh water flux associated with river runoff. These conditions, and the lack of vertical mixing below the surface mixed layer, provide an ideal environment for the formation of double diffusive staircases.

### C. EARLIER ESTIMATES OF HEAT FLUX

The fluxes associated with double diffusion have been studied extensively. It is generally accepted that in systems characterized by active diffusive layering, the interaction between layers is controlled by the flux of salt and heat across the diffusive interfaces. Based on a set laboratory experiments the balance of temperature variation between adjacent layers and heat flux (Turner, 1973) was proposed as follows.

$$\alpha F_T = A_1 \cdot (\alpha \Delta T)^{\frac{4}{3}} \quad (1)$$

$$R_\rho = \frac{\beta \Delta S}{\alpha \Delta T} \quad (2)$$

This relationship (1) has since been known as the 4/3 flux law.  $A_1$  has the dimensions of velocity and is a

function of the density ratio ( $R_\rho$ ).  $F_T$  is temperature flux,  $\alpha$  is the thermal expansion coefficient, and  $\beta$  is the saline contraction coefficient.

The 4/3 flux law states that the fluxes associated with double diffusion are controlled entirely by the variation in temperature or salinity across the diffusive interface and is independent of layer thickness. The lack of sensitivity of fluxes to vertical scales is critically important to our observation-based study because the thickness of an interface is often much smaller (<25cm) than the resolution of the sensor, whereas, a difference in mean temperatures of each layer can easily be measured. Dimensional analysis suggests that the 4/3 flux law can be written as follows:

$$\alpha F_T = C(R_\rho) \cdot \left( \frac{g \kappa_T^2}{\nu} \right)^{\frac{1}{3}} \cdot (\alpha \Delta T)^{\frac{4}{3}} \quad (3)$$

$C(R_\rho)$  is an unknown constant,  $g = 9.8 \text{ m/s}^2$ ,  $\nu = 1.8 \times 10^{-6} \text{ m}^2/\text{s}$  is the kinematic viscosity,  $\kappa = 1.4 \times 10^{-7} \text{ m}^2/\text{s}$  is the molecular diffusivity of heat.

Marmorino and Caldwell (1976) examined the 4/3 flux law in depth. They discovered an empirical formulation of the coefficient  $C(R_\rho)$  using the following equations:

$$\frac{H}{H_{sp}} = 3.8 R_\rho^{-2} \quad (4)$$

$$H_{sp} = (0.085) k_T \left( \frac{g \alpha}{\kappa \nu} \right)^{\frac{1}{3}} \Delta T^{\frac{4}{3}} \quad (5)$$

$$\frac{H}{H_{sp}} = 0.101 \exp \left\{ 4.6 \exp \left[ -0.54 (R_\rho - 1) \right] \right\} \quad (6)$$

$$C(R_\rho) = 0.00859 \exp\left(4.6 \exp\left[-0.54\{R_\rho - 1\}\right]\right) \quad (7)$$

Using Huppert's formula (4), they were able to determine a relationship between the measured heat flux (H) and (5), the theoretical heat flow through a non-deformable interface ( $H_{sp}$ ). They proposed a new formulation also based on laboratory experiments (6), which ultimately yielded a value for  $C(R_\rho)$ .

The coefficient  $C(R_\rho)$  has since been scrutinized, most notably by Kelley (1990). In his 1990 paper, Kelley proposed a new value for  $C(R_\rho)$  based on what he referred to as a full collection of laboratory measurements. He analyzed laboratory experiments for  $1 \leq R_\rho \leq 10$ , while Turner (1973) only looked at values of  $R_\rho$  up to 7.

$$C(R_\rho) = 0.0032 \exp\left(\frac{4.8}{R_\rho^{0.72}}\right) \quad (8)$$

Equation (8) is the result of Kelley's laboratory experiments, and along with (7), the two have been used interchangeably as a standard method for calculating fluxes using the 4/3 flux law. However, Kelley suggested that perhaps the 4/3 exponent is incorrect and should be changed to 5/4. Additional experimentation is required to support this proposition.

Padman and Dillon (1987) showed that using the Marmorino and Caldwell formulation of the 4/3 flux law, they could calculate the fluxes in the Beaufort Sea. Their results showed that those fluxes were  $0.02 - 0.1 \text{ Wm}^{-2}$ . A more recent study (Timmermans, 2008), also based on extrapolation of laboratory derived results, estimated the

heat flux associated with the diffusive staircases as measured by the Ice Tethered Profilers to be  $0.22 \pm 0.10$  W/m<sup>2</sup>.

Wilson (2007) compared the two formulations (7) and (8) using data collected via the Ice Tethered Profilers, a set of moored CTDs in the Beaufort Sea, which will be discussed in detail in Chapter II. She found that in order to fit the data collected in the Beaufort Sea to these formulae each needed to be multiplied by a transfer coefficient. She suggested that the laboratory results of both Kelley (1990) and Marmorino and Caldwell (1976) cannot be applied to actual data collected in the field, and perhaps the laboratory measurements require calibration prior to application in the Arctic. She concluded that the average heat flux in the Beaufort Gyre in excess of  $1 \text{ Wm}^{-2}$ . This is significantly larger than estimates using the original  $4/3$  flux law.

Caro (2009) used a set of high-resolution numerical experiments to validate some of the conclusions made by Wilson. He used two-dimensional numerical models to estimate the heat fluxes in the Beaufort. His efforts resulted in fluxes on the order of  $1 \text{ W/m}^2$ .

Timmermans' findings differ from Wilson's (2007) and Caro's (2009) by an order of magnitude, and in some cases Padman and Dillon's differ by two orders of magnitude. Such a wide range of estimates in a region critically important for climate variability provides the impetus for this study. This thesis attempts to resolve the controversy in assessment of the vertical heat transport by applying inverse modeling techniques to observations.



#### D. INVERSE MODELING

The study of the oceans traditionally follows two distinct directions. One involves numerical modeling and theoretical manipulation of the equations governing dynamics and thermodynamics of the sea. The other is observationally oriented, where real measurements are discussed in the context of qualitative physical principles.

As oceanography matures into a quantitative science, it becomes increasingly desirable to connect the observational and modeling aspects of the field. Laboratory experiments often attempt to bridge this gap between hard facts and theoretical deductions. Laboratory researchers strive to replicate the ocean environment as closely as possible, but exact correspondence is seldom achieved, given the substantial differences in the conditions and spatial scales between the laboratory and nature.

Another more recent approach, which makes it possible to connect data with theory, involves inverse modeling. Inverse models attempt to directly calculate model parameters from observations by minimizing errors associated with observational measurements and fitting those measurements to the governing equations. In our case, temperature, salinity and depth measurements were taken by the Ice Tethered Profilers, and velocity and diffusion coefficients are calculated from those observations using the method of Total Least Squares.

$$\nabla \cdot (\mathbf{V}T) + \frac{\partial wT}{\partial z} = \frac{\partial}{\partial z}(F_T) \quad (9)$$

$$\nabla \cdot (\mathbf{V}S) + \frac{\partial wS}{\partial z} = \frac{\partial}{\partial z}(F_S) \quad (10)$$

$$\nabla \cdot \mathbf{V} + \frac{\partial w}{\partial z} = 0 \quad (11)$$

The inverse model in this study is based on the static advective diffusive (9), (10) and mass continuity equations (11) in divergence form.  $F_T$ , and  $F_S$  is the temperature or salinity flux. The formulation of  $F_T$  and  $F_S$  is central to this study. In this work we examine flux-gradient formulations in which  $F_T$ , and  $F_S$  are assumed to be controlled by the background temperature and salinity gradients, as well as the interfacial flux laws. Results of both are qualitatively consistent, but differ in details.

#### **E. UNRESOLVED ISSUES**

This thesis attempts to quantify the heat flux associated with diffusive convection independent of the extrapolation of laboratory derived laws. This information is used to address the following questions.

1. What are the typical vertical heat and salt fluxes in the diffusive staircases in the Beaufort Gyre? Vertical heat fluxes of  $0.02 - 6 \text{ Wm}^{-2}$  represent an extremely wide range making it difficult to assess the large-scale consequences of heat transfer in the Arctic. If the value is less than  $1 \text{ Wm}^{-2}$ , then it is likely that the heat delivered upward vis-à-vis diffusive convection is not a major contributor to sea ice melt. However, if Wilson (2007) is correct, then diffusive convection is sufficient to affect the pattern on stratification and ocean climate in the Arctic.

2. Can the heat flux through the diffusive staircases significantly contribute to the heat imbalance associated with the melting of the polar ice cap?

3. What are the relative roles of the vertical and lateral transport of heat in Beaufort gyre? Is it possible to capture the zero-order dynamics at play by a one-dimensional horizontally averaged model?

4. Is it possible to accurately evaluate fluxes associated with double diffusion by inverse modeling techniques? Lee and Veronis (1991) showed that it is possible to quantify the fluxes via an inverse model using the method of Total Least Squares in the tropical Atlantic Ocean. A similar inverse model of the advective-diffusive equations is applied to data collected from 2004-2009 via the Ice Tethered Profilers operated by the Woods Hole Oceanographic Institute. Using methods described in Lee and Veronis (1991) the inverse technique is implemented to determine eddy diffusivity coefficients using the method of total least squares. A comparison to the estimates using the  $4/3$  flux laws described in Timmermans (2008) and Padman and Dillon (1987) is discussed along with a comparison to Wilson (2007), additionally the results of this study area compared to the model results from Caro (2009).

This thesis is organized as follows: Chapter II reviews the data from the Ice Tethered Profilers and some of the unique processing required for obtaining the appropriate data set for the inverse calculation. Chapter III offers a detailed description of the mathematical foundation of the inverse model as well as its application to the ITP data set. Chapter IV presents the results of four models, the one dimensional (vertical only) model, which uses an average single profile to determine fluxes, and three variations of a full three dimensional model. A discussion of the findings and conclusions is in Chapter V.

## II. DATA AND DATA PROCESSING

### A. ICE-TETHERED PROFILER DATA

The Woods Hole Oceanographic Institute (WHOI) Ice Tethered Profiler (ITP) program was established in 2004 to provide timely and accurate oceanographic measurements in the Arctic Ocean. Historically, access to the ice covered Arctic Ocean has been limited. The ITPs assist in assuring consistent measuring capability in a data-sparse environment. Between 2004 and 2006, the first six ITPs were deployed in the Beaufort Sea. Data from ITPs 1-6 are used in this study. As of July 2009, these six sensors collected over 7000 profiles, all of which have been made available to the public.

The ITP is a moored conductivity, temperature, and depth (CTD) sensor. Each one is designed to move with the ice it is moored to and has the potential lifespan of approximately three years. The ITP consists of a small platform on top of which rests a buoy. A 10-inch hole is drilled through the sea ice and the instrument is inserted in the water from above. The instrumentation is tethered to the surface float via a wire rope that is weighted on the bottom. This rope is approximately 800 meters in length, and the instrument traverses the wire rope several times daily.

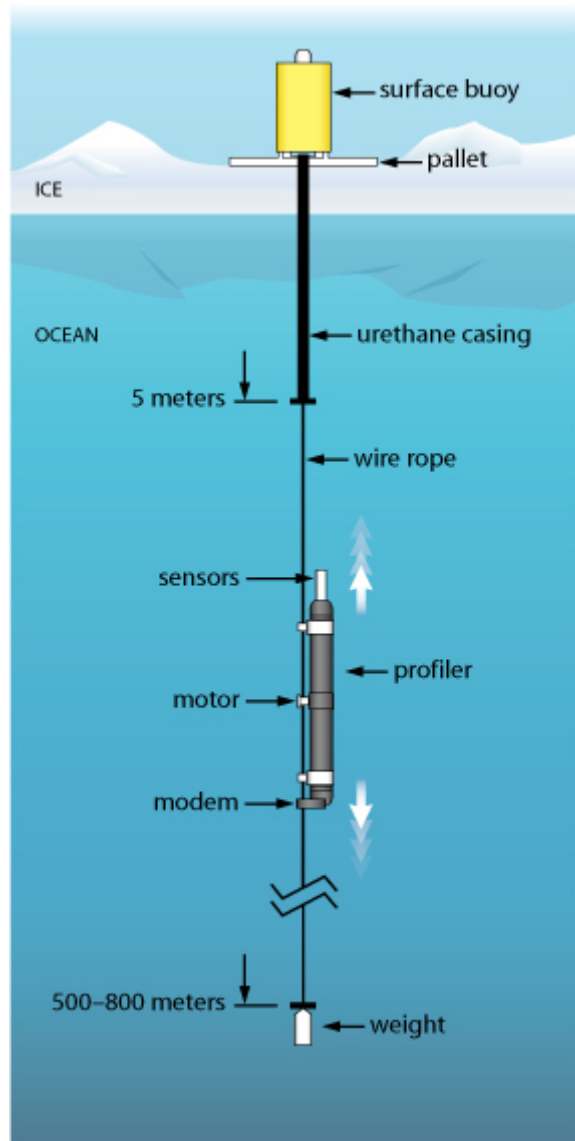


Figure 4. Ice tethered profiler system

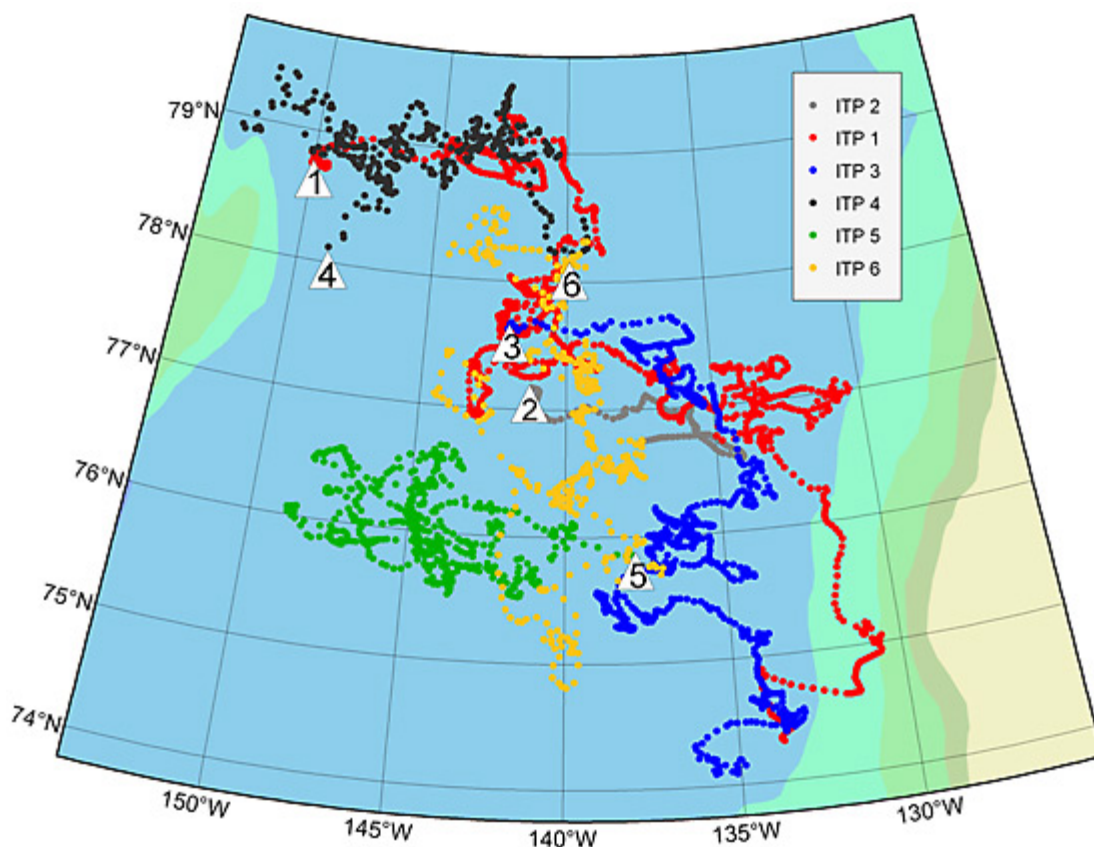


Figure 5. Location of ITP 1-6

Figure 4 illustrates the ITP system and Figure 5 presents the trajectories of the first six profilers followed over their lifespans. The data used in this study are labeled "Level 3 Archive Data" by WHOI. This form of data represents the best possible representation of the ocean properties as measured by the ITPs. Corrections have been applied that account for sensor response, regional conductivity variation, and quality assurance. Each data file is formatted to be compatible with MATLAB. Each profile was retrieved via <ftp://ftp.whoi.edu/whoinet/itpdata/> and processed further as described below.

## **B. DATA PROCESSING**

The corrected ITP data described above was arranged by profiler number 1-6 and processed together as one data set. Processing began with the corrected ITP data obtained from the WHOI ITP Web site. Wilson (2007) suggested that anomalous results were obtained from the profiles corresponding to the downward data collection for each cast. This is possibly due to sensor contamination associated with the main ITP sensor platform below the sensor suite. As the profiler is lowered into the water the platform interacts with the water just below the sensors, affecting the measurements. Based on this suggestion, all downward collected profiles were removed from the total dataset, effectively reducing the amount of data by half.

Diffusive convection occurs in the thermocline region of the Beaufort Sea between approximately 200 meters and 400 meters depth, with the majority of the diffusive layers in the upper 100 meters of the thermocline. The data were then reduced to only those data from 200 db pressure to 300 db pressures, which correspond to roughly 195 meters to 295 meters depth. All temperatures were converted to potential temperature. Table 1 summarizes the remaining data. Each profile consists of temperature, salinity, pressure, and depth measurements.

ITP	Max # of Obs in each Profile	# of Profiles
1	1051	1022
2	520	122
3	1987	766
4	1917	349
5	2327	547
6	1710	667

Table 1. Number of Observations (individual data points) for Each Profile. Each profile has up to the maximum number of observations indicated. Not all profiles have the maximum number of observations.

These data were further reduced by determining the values of temperature and salinity at the center of each layer. This was accomplished by searching the data for the local maxima of vertical temperature gradient. This local maximum corresponds to the interface between each layer. Using the position of each interface, the center of each layer is determined to be exactly half way between two adjacent interfaces. The temperature, salinity and depth of these data points is recorded and marked. Table 2 shows the number of individual diffusive layers found in the data organized by profiler.

ITP	# of Layers	# of Profiles
1	48	1022
2	39	122
3	51	766
4	54	349
5	51	547
6	62	667

Table 2. Number of Layers for Each Profile.



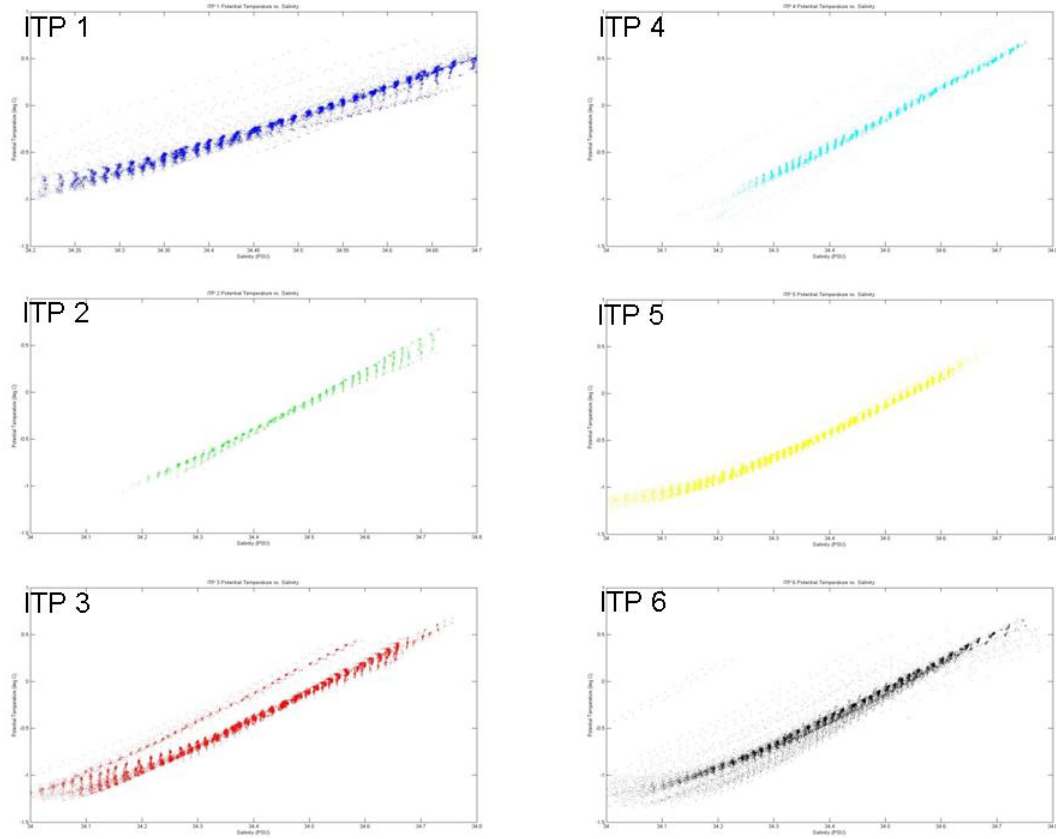
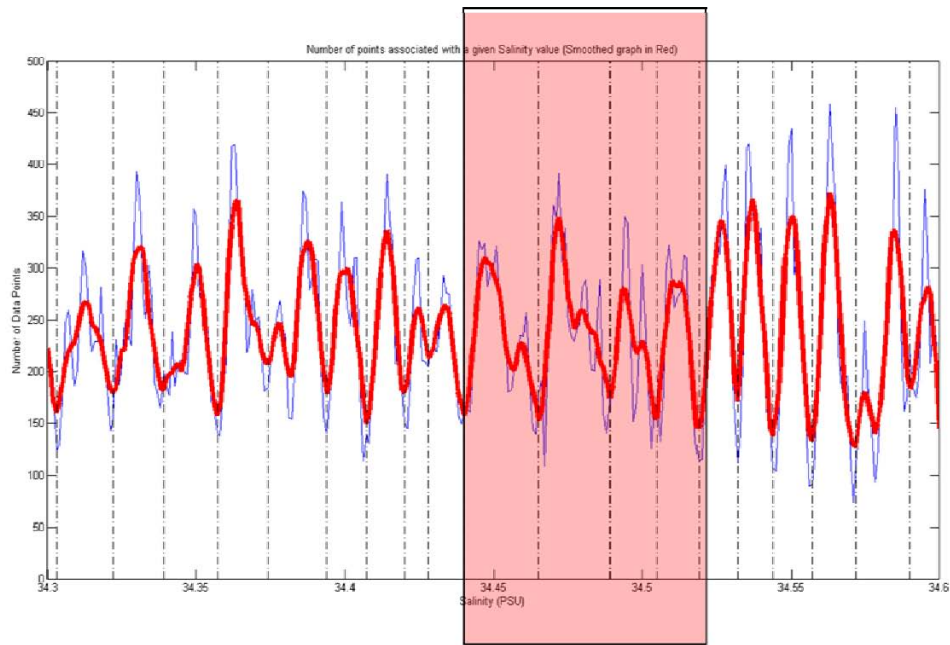


Figure 6. Temperature - Salinity plot for ITPs 1-6.

The diffusive layers next must be classified independently of the particular cast. Timmermans (2008) showed that each diffusive layer can be identified via a plot of potential temperature versus salinity. Figure 6 is a Temperature-Salinity plot for each ITP used in this study. The vertical clusters at nearly constant salinity are associated with a horizontally homogeneous layer, a diffusive layer. Due to the remarkable lateral coherence of layers in the thermohaline staircase, it is possible to consolidate the data into one dataset by identifying pronounced layers that appear in all six datasets.



**Highly variable structure may  
result in spurious results**

Figure 7. Histogram of data: Number of data points for a given salinity value.

Using a moving window across salinity space that corresponds to a 0.001 PSU increment from 34.3 PSU to 34.6 PSU we estimated the concentration of data points as a function of salinity, as shown in Figure 7. The blue curve is the original histogram. The red curve is a 5-point moving average, which is used to identify the individual layers. Noting that the concentration of points is highest at the center of the layers and lowest at the interface, we assume that the troughs in the histogram represent the boundary (interface) between each layer. The black dashed lines represent the inferred interface locations.

ITP	# of Layers	# of Profiles
1	19	1022
2	19	122
3	19	766
4	19	349
5	19	547
6	19	667
ALL	19	3452

Table 3. Total number of layers and profiles in final data set.

These values are used to enumerate layers in all profiles. The result is a total of 19 layers common to each profiler (Table 3). The data between adjacent troughs (dashed lines in Figure 7) are considered to be in the same layer. Thus, layer 1 contains data only from the region between the first two troughs on the left of the graph. Layer 1 corresponds to the shallowest layer in the thermocline, and layer 19 corresponds to the deepest (as salinity increases downward). It is important to note that diffusive layers in the Beaufort Sea are not limited to these 19. These are the layers that are common to all 6 ITPs used in this study.

The highlighted portion of Figure 7 shows the difficulty in capturing each layer accurately. The blue line clearly shows a highly variable structure in this region, and our method for determining the interfaces between adjacent layers is not precise enough to account for this variation. As a result, we observed some anomalous results in the inverse calculations.

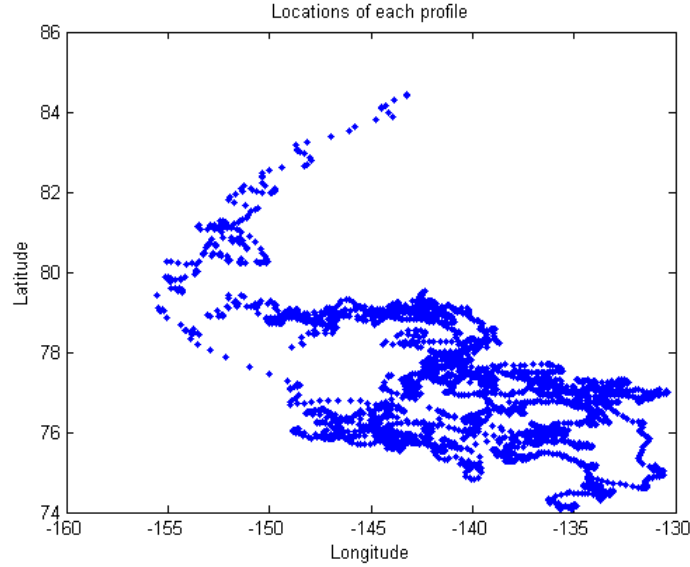


Figure 8. Locations of each profile.

Ultimately, each profile yielded a specific value of temperature, potential temperature, salinity, layer thickness, depth, pressure, and latitude and longitude for each of the 19 layers. Figure 8 is a plot of the locations of all 3452 profiles. The next step involves interpolation of the data onto a structured grid for use with the inverse model.

### C. INTERPOLATING DATA TO A GRID

The inverse model used in this study requires the data to be applied to an equidistantly spaced grid in both horizontal directions. This is accomplished using the MATLAB routine "griddata," which linearly interpolates the data to a pre-determined set of grid coordinates. The result is a dataset that is compatible with the inverse model. The horizontal length scale is 15 km, both zonal and meridional, unless otherwise noted. The vertical length scale is defined by the layer thickness at each location.

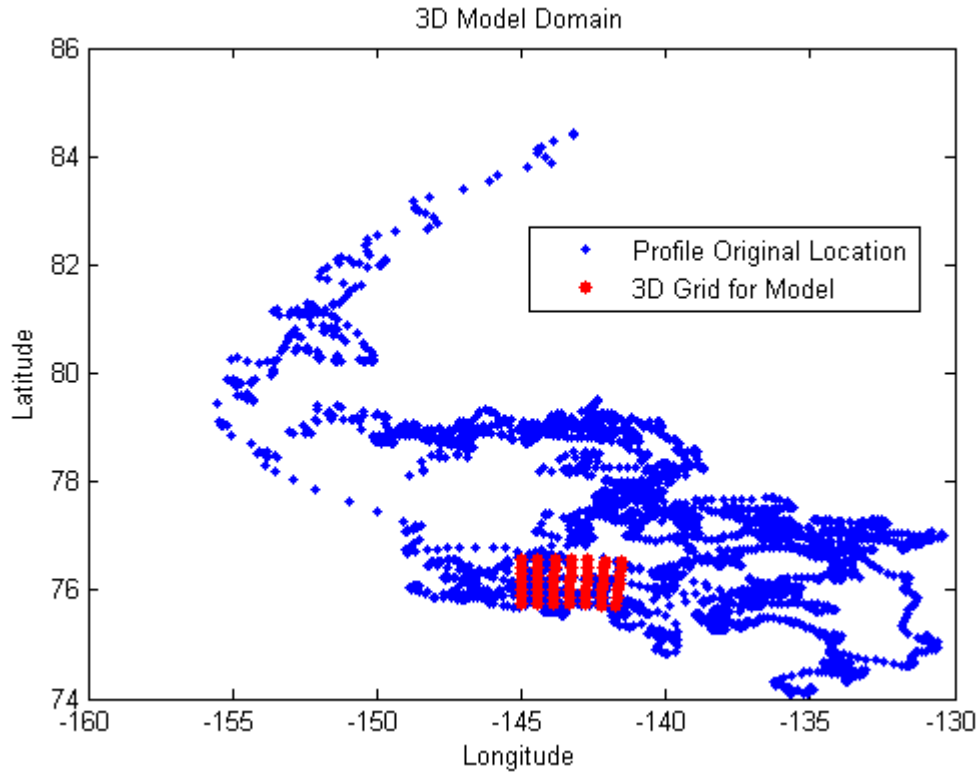


Figure 9. Location of the three-dimensional dataset.

The grid used for the three dimensional model has the dimensions 7X7X19. Figure 9 shows the location of the grid. This location in the southern Beaufort Sea was chosen because of the high density of original profile locations, as well as the relatively even distribution of profiles throughout the grid domain.

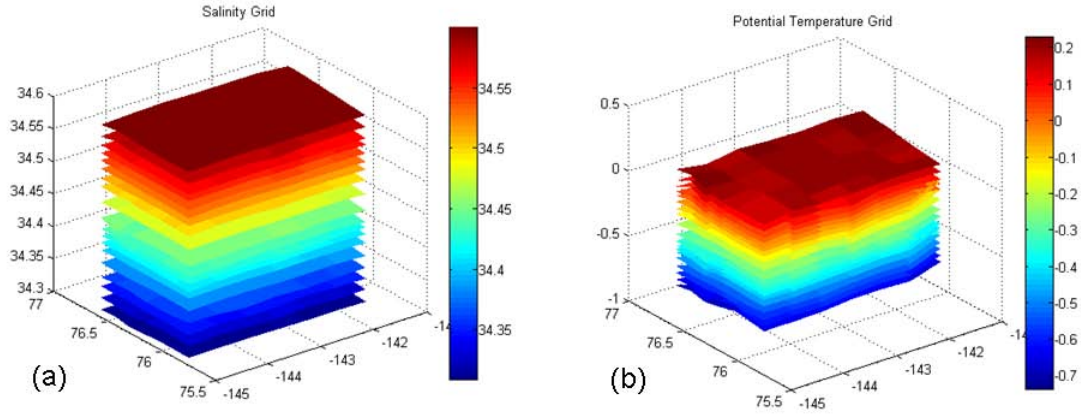


Figure 10. (a) Salinity surfaces for 19 layers used in the inverse calculation. (b) The corresponding potential Temperature surfaces.

The structured data are shown in Figure 10, which reveals nearly constant temperature and salinity values in each of the diffusive layers, and the lateral coherence of those layers over of the model domain. For both Figures 10a and 10b, the layers are arranged from the deepest to the shallowest from top to bottom. The salinity values for each layer are nearly constant spatially. The temperature values vary slightly, but the homogeneity is evident.

THIS PAGE INTENTIONALLY LEFT BLANK

### III. INVERSE MODEL

#### A. MODEL FRAMEWORK

In order to apply (9), (10) and (11) to measurements they must be discretized in space. This is achieved by integrating vertically from the bottom (b) to the top (t) of each layer, assuming vertically uniform temperature and salinity within each layer, consistent with characteristic properties of diffusive convection in thermohaline staircases.

$$\nabla \cdot \left( \tilde{\mathbf{V}} T \right) + [wT - F_T]_b^t = 0 \quad (12)$$

$$\nabla \cdot \left( \tilde{\mathbf{V}} S \right) + [wS - F_S]_b^t = 0 \quad (13)$$

$$\nabla \cdot \tilde{\mathbf{V}} + [w]_b^t = 0 \quad (14)$$

$\tilde{\mathbf{V}}$  represents the vertically integrated horizontal velocity along the layer, and  $w$  represents the vertical velocity across the interface. The vertical influences into and out of each layer are described by the diffusive and convective terms in (12) and (13) (Lee et al., 1991).

The inverse model is based on the optimal solution to the overdetermined linear system of equations  $\mathbf{Ax}=\mathbf{b}$ . Literature refers to  $\mathbf{A}$  as the data matrix and  $\mathbf{b}$  as the observation vector. We will follow this same convention in this study. The solution is  $\mathbf{x}$ , a vector with the same dimensions as  $\mathbf{b}$  where each component of  $\mathbf{x}$  represents the coordinates of  $\mathbf{b}$  in terms of the columns of  $\mathbf{A}$ .



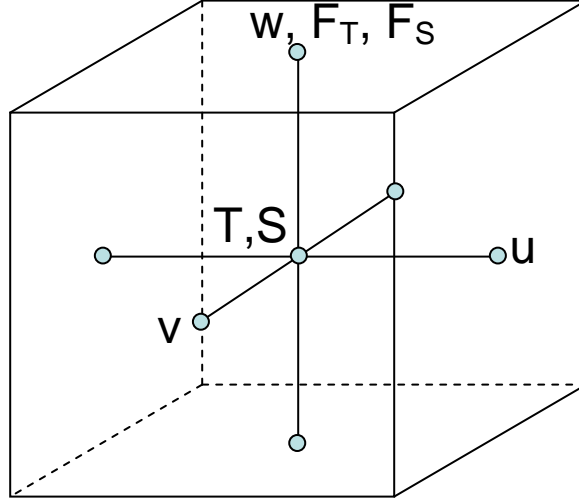


Figure 11. The seven-point grid network for finite differencing. (After Lee & Veronis, 1991)

To formulate the problem in terms of the algebraic, rather than the differential system the governing equations are discretized in three dimensions using centered finite-differencing on a seven-point grid (Figure 11). Each cell in the grid has the measured tracer value, temperature and salinity, in the center,  $u$  and  $v$  on the lateral boundaries and  $w$ ,  $F_T$  and  $F_S$  on the vertical boundaries.

$$\begin{aligned}
& \frac{(T_0 + T_{i+1})(h_0 + h_{i+1})}{2l_x} u_{i+\frac{1}{2}} - \frac{(T_{i-1} + T_0)(h_{i-1} + h_0)}{2l_x} u_{i-\frac{1}{2}} \\
& + \frac{(T_0 + T_{j+1})(h_0 + h_{j+1})}{2l_y} v_{j+\frac{1}{2}} - \frac{(T_{j-1} + T_0)(h_{j-1} + h_0)}{2l_y} v_{j-\frac{1}{2}} \\
& + \frac{2(h_{k+1}T_0 + h_0T_{k+1})}{h_0 + h_{k+1}} w_{k+\frac{1}{2}} - \frac{2(h_0T_{k-1} + h_{k-1}T_0)}{h_{k-1} + h_0} w_{k-\frac{1}{2}} \\
& + 2 \left( F_{T_{k+\frac{1}{2}}} \right) - 2 \left( F_{T_{k-\frac{1}{2}}} \right) = 0
\end{aligned} \tag{15}$$

$$\begin{aligned}
& \frac{(S_0 + S_{i+1})(h_0 + h_{i+1})}{2l_x} u_{i+\frac{1}{2}} - \frac{(S_{i-1} + S_0)(h_{i-1} + h_0)}{2l_x} u_{i-\frac{1}{2}} \\
& + \frac{(S_0 + S_{j+1})(h_0 + h_{j+1})}{2l_y} v_{j+\frac{1}{2}} - \frac{(S_{j-1} + S_0)(h_{j-1} + h_0)}{2l_y} v_{j-\frac{1}{2}} \\
& + \frac{2(h_{k+1}S_0 + h_0S_{k+1})}{h_0 + h_{k+1}} w_{k+\frac{1}{2}} - \frac{2(h_0S_{k-1} + h_{k-1}S_0)}{h_{k-1} + h_0} w_{k-\frac{1}{2}} \\
& + 2 \left( F_{S_{k+\frac{1}{2}}} \right) - 2 \left( F_{S_{k-\frac{1}{2}}} \right) = 0
\end{aligned} \tag{16}$$

$$\frac{h_0 + h_{i+1}}{2l_x} u_{i+\frac{1}{2}} - \frac{h_{i-1} + h_0}{2l_x} u_{i-\frac{1}{2}} + \frac{h_0 + h_{j+1}}{2l_y} v_{j+\frac{1}{2}} - \frac{h_{j-1} + h_0}{2l_y} v_{j-\frac{1}{2}} + w_{k-\frac{1}{2}} - w_{k+\frac{1}{2}} = 0 \tag{17}$$

The model discretization is employed exactly as described in Lee and Veronis (1991). Equations (15), (16) and (17) are the discretized forms of the advective diffusive equations and the continuity equation respectively. The indices  $i$ ,  $j$ ,  $k$  represent the location of the tracer for that grid cell, where  $i$  increases eastward,  $j$  increases northward, and  $k$  increases downward with depth. The  $\frac{1}{2}$  values correspond to the boundaries of the grid cell. Velocities and diffusive fluxes into and out of each cell are calculated at the boundary between grid cells. Thus, the coefficients are weighted averages of thickness and tracer values at each corresponding boundary. Slight variations are used in the three-dimensional models as we explore different formulations of flux calculations. These variations are described in Chapter IV.

Notice that the integrated forms of the original equations are homogeneous. Thus, the model will have an exact trivial (zero) solution. To avoid this unphysical solution one must introduce a known, or estimated, quantity that can be used to populate a non-zero observation vector

**b.** This known quantity will be referred to as the reference unknown  $x_r$ . To illustrate the concept of a reference variable consider a homogeneous system ( $\mathbf{b}=0$ ) of four equations with three unknowns.

$$\begin{pmatrix} 1+\varepsilon & 2-\varepsilon & 3+\varepsilon \\ 4-\varepsilon & 2+\varepsilon & 7-\varepsilon \\ 8+\varepsilon & 1-\varepsilon & 5+\varepsilon \\ 6-\varepsilon & 5+\varepsilon & 3+\varepsilon \end{pmatrix} \begin{pmatrix} x_1 \\ x_2 \\ x_3 \end{pmatrix} = \begin{pmatrix} 0 \\ 0 \\ 0 \\ 0 \end{pmatrix} \quad (18)$$

Let us assume that the value of  $x_1$  is known or can be readily estimated with some degree of certainty. All of the equations can be divided by  $x_1=x_r$ . This effectively forces an inhomogeneous term where  $\mathbf{b} \neq 0$  and creates a non-trivial solution to the problem.

$$\begin{pmatrix} 2-\varepsilon & 3+\varepsilon \\ 2+\varepsilon & 7-\varepsilon \\ 1-\varepsilon & 5+\varepsilon \\ 5+\varepsilon & 3+\varepsilon \end{pmatrix} \begin{pmatrix} x_2/x_1 \\ x_3/x_1 \end{pmatrix} = - \begin{pmatrix} 1+\varepsilon \\ 4-\varepsilon \\ 8+\varepsilon \\ 6-\varepsilon \end{pmatrix} \quad (19)$$

Lee (1991) showed that this is an effective method to produce the inhomogeneous terms that are necessary for the inverse calculations. The model, however, is very sensitive to the choice of reference variable. This sensitivity is explored in Chapter IV.

Another essential step to obtain a reliable solution to the problem is to ensure that the system of equations is overdetermined, i.e., that we have more equations than unknowns. This acts to smooth out the errors in the data. Each grid cell contains three equations, two tracer (temperature and salinity) equations, and continuity. As written, there are three equations and five unknowns,  $u$ ,  $v$ ,

$w$ ,  $F_S$ , and  $F_T$ . Two important assumptions are made to ensure that there are fewer unknowns than equations. The first assumption is that  $w$ ,  $F_S$  and  $F_T$  are constant at each interface, and the second is that  $w$  at the top layer is equal to Ekman pumping velocity ( $w_e \approx 5 \times 10^{-7}$  m/s) at the top of the thermocline (Yang, 2006). This ensures that the system is overdetermined. In our case, we have 1275 equations and 1073 unknowns

Finally, the data matrix  $\mathbf{A}$  and the observation vector  $\mathbf{b}$  are built using the coefficients in (15), (16) and (17). This is accomplished by populating a matrix with the coefficients of the model unknowns in the correct location. Each equation is represented by a specific row and each unknown by a specific column. The result is a very sparse matrix, where most of the values in the matrix are zero.

$$\mathbf{A} = \begin{pmatrix} \text{coeff}(u_1) & \text{coeff}(u_2) & 0 & \dots & \dots & 0 & \dots \\ 0 & \text{coeff}(u_2) & \text{coeff}(u_3) & 0 & \dots & 0 & \dots \\ 0 & 0 & \text{coeff}(u_3) & \text{coeff}(u_4) & \dots & 0 & \dots \\ 0 & 0 & 0 & \ddots & \ddots & 0 & \dots \\ 0 & 0 & 0 & 0 & \text{coeff}(u_n) & \text{coeff}(u_{n+1}) \dots \end{pmatrix} \quad (20)$$

Equation (20) is an example of the structure of the 3-dimensional form of the data matrix  $\mathbf{A}$ , and  $n$  corresponds to the number of  $u$  unknowns. A similar pattern continues for the coefficients of  $v$ ,  $w$ ,  $F_T$ , and  $F_S$  completes the matrix. In our case  $\mathbf{A}$  has the dimensions 1275 rows (equations) X 1073 columns (unknowns).

The reference unknown and its corresponding coefficients are divided through as shown in (19), and the vector  $\mathbf{b}$  is obtained by subtracting the coefficients for the

reference variable from both sides of the equation. The basic framework for the TLS method and the inverse calculation is now complete.

## B. THE "BEST" SOLUTION TO THE OVERDETERMINED SYSTEM

The methods for solving  $\mathbf{Ax}=\mathbf{b}$ , where the data matrix  $\mathbf{A} \in R^{m \times n}$  and the observation vector  $\mathbf{b} \in R^n$  are given, are relatively well known. Specifically, when  $m > n$  and therefore  $\mathbf{Ax}=\mathbf{b}$  is an over determined system; i.e., one that has more equations than unknowns, there is generally no exact solution. In such cases then, one attempts to formulate a "close" problem that is exactly solvable.

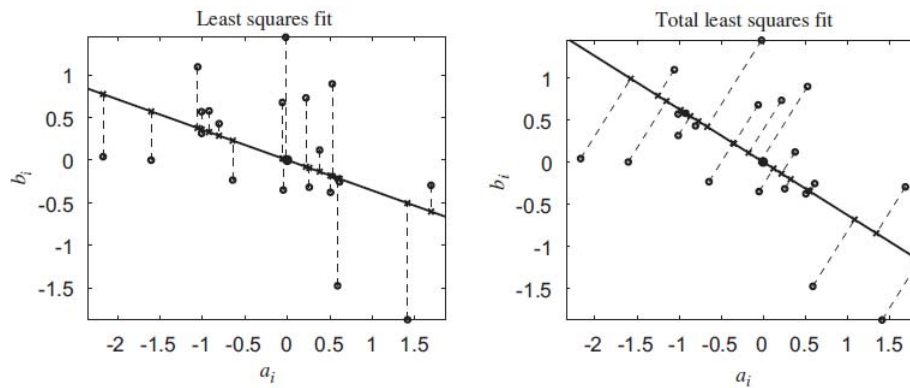


Figure 12. Least squares and total least squares fits of a set of  $m=20$  data points in the plane and just one unknown  $\mathbf{x}$ .  $\mathbf{a}_i$  and  $\mathbf{b}_i$  represent the components of an example data matrix  $\mathbf{a}$  and an observation vector  $\mathbf{b}$ . In the least squares fit the error only exists in  $\mathbf{b}$  and in the total least squares fit errors exist in both  $\mathbf{a}$  and  $\mathbf{b}$ . (From Markovsky et al., 2007)

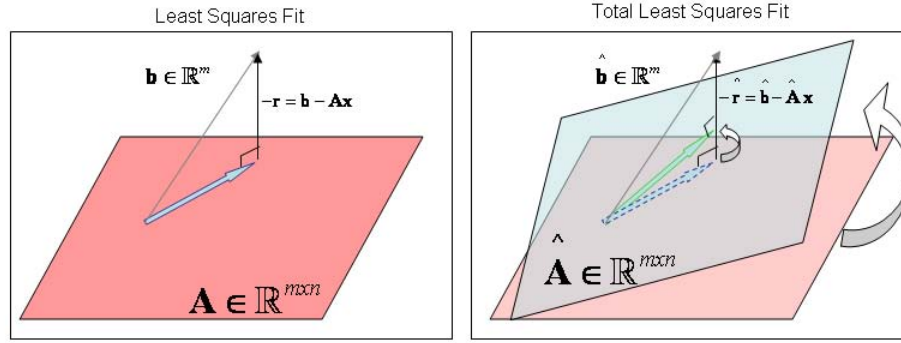


Figure 13. Least Squares and Total Least Squares fits of a plane  $\mathbf{A}$  and vector  $\mathbf{b}$ . The plane  $\mathbf{A}$  is a representation of all possible values for  $\mathbf{Ax}$ . Ultimately only one vector  $\mathbf{Ax}$  represents the closest approximation of  $\mathbf{b}$ .

(a) LS minimizes the vector  $-\mathbf{r}$ , where  $-\mathbf{r}$  only represents error in the vector  $\mathbf{b}$ , by projecting  $\mathbf{b}$  onto the plane  $\mathbf{A}$ . (b) TLS minimizes  $-\mathbf{[E|r]}$  which represents the error in both  $\mathbf{A}$  and  $\mathbf{b}$ , needed to project  $\mathbf{b}$  onto the perturbed plane  $\mathbf{A}$ . Both the data matrix and the observation vector are corrected to find an exact solution.

The classical method of Least Squares attempts to find a "best" solution by assuming that no exact solution exists entirely due to error in the observations.  $\mathbf{A}$  in theory is assumed to be precisely correct and some small correction  $\mathbf{r}$  exists such that  $\mathbf{Ax}=\mathbf{b}+\mathbf{r}$  is exactly solvable. (In this case  $-\mathbf{r}$  represents the errors in the observation vector.) The solution of the problem is a vector  $\mathbf{x} \in \mathbb{R}^n$  corresponding to the minimum correction required to make the problem solvable, i.e.  $\min_{\mathbf{x} \in \mathbb{R}^n} \|\mathbf{Ax} - \mathbf{b}\|_2 = \min_{\mathbf{x} \in \mathbb{R}^n} \|\mathbf{r}\|_2$ . Geometrically, the solution represents either minimizing the sum of the squared vertical distances from the data points to the fitting curve (Figure 12a), or the projecting the data vector onto the plane spanned by the columns of  $\mathbf{A}$  (Figure 13a).

The total least squares method is an extension of the classical Least Squares technique that takes into account

errors in both the data matrix  $\mathbf{A}$  and the observation vector  $\mathbf{b}$  (Golub et al., 1980). The method assumes that only  $(\mathbf{A}+\mathbf{E})\mathbf{x}=\mathbf{b}+\mathbf{r}$  is exactly solvable.  $\mathbf{E}$  represents the correction in the data matrix  $\mathbf{A}$  and  $\mathbf{r}$  represents the correction in the observation vector  $\mathbf{b}$ .

$$\|[\mathbf{E}|\mathbf{r}]\|_F = \sqrt{\sum_{i=1}^m \sum_{j=1}^n |[\mathbf{E}|\mathbf{r}]_{ij}|^2} \quad (21)$$

The solution corresponds to making the minimum correction in the sense that  $\min_{\mathbf{b}+\mathbf{r} \in \mathbf{R}^{(\mathbf{A}+\mathbf{E})}} \|[\mathbf{E}|\mathbf{r}]\|_F$ , where  $\|\bullet\|_F$  denotes the Frobenius norm, and  $\mathbf{E} \in \mathbf{R}^{m \times n}$  and  $\mathbf{r} \in \mathbf{R}^n$ . The Frobenius norm is defined as square root of the sum of the absolute squares of the elements of the matrix (21).

Geometrically, the total least squares solution can be described as either minimizing the sum of the squared orthogonal distances from the data points to the fitting curve (Figure 12b), or the projecting the data vector onto the plane spanned by the columns of  $\mathbf{A}+\mathbf{E}$  (Figure 13b).

The Total Least Squares and Least Squares methods are shown schematically in Figure 12 and Figure 13. The difference in the solutions for the two methods amounts to changing both the slope of the line and the intercept (Figure 12), or adjusting both the plane  $\mathbf{A}$  and vector  $\mathbf{b}$  (Figure 13) to find a solution, represented by the fit line in Figure 12 and the colored vectors on the plane in Figure 13.

There are two other important characteristics of the TLS solution to consider. First, the method implicitly assumes that the values of the data matrix  $\mathbf{A}$  and observation vector  $\mathbf{b}$  are roughly the same. In Figure 12, the range of

$\mathbf{a}_i$  and  $\mathbf{b}_i$  are roughly the same, approximately -2 to 2. This is important to limiting the sensitivity of the solution since the method of TLS makes absolute, not relative, changes to  $\mathbf{A}$  and  $\mathbf{b}$ . If the range of each input matrix is nearly the same, then the norm of the solution vector  $\mathbf{x}$  will be approximately 1. If there are one or more orders of magnitude difference in the range of the data matrix  $\mathbf{A}$  and observation vector  $\mathbf{b}$  then it is likely that the solution to the total least squares problem will be greatly different from the least squares problem. A large difference between TLS and LS can be interpreted as a warning sign that the solution may be physically inconsistent, as illustrated in Figure 14. A difference by a factor of four in the norms of  $\mathbf{A}$  and  $\mathbf{b}$  can result in dramatic differences in solutions.

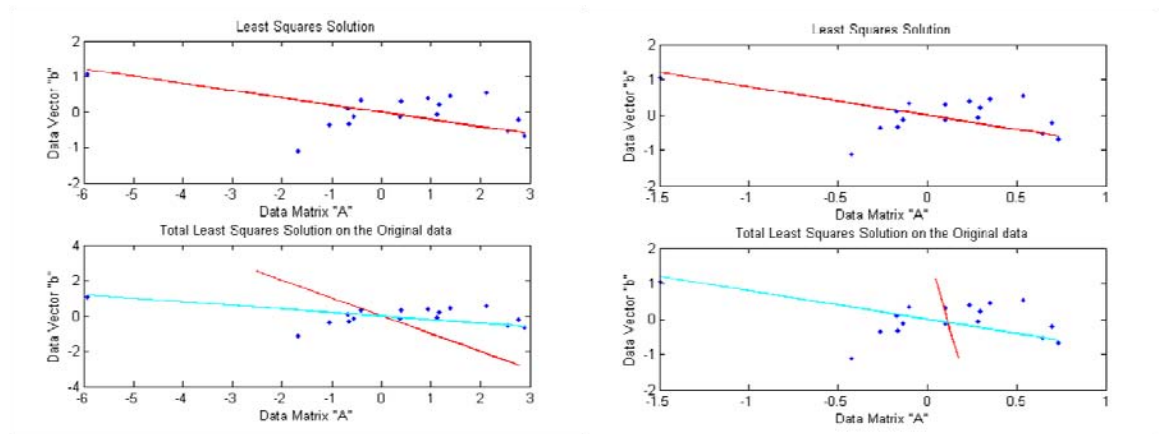


Figure 14. The importance of similar norms for  $\mathbf{A}$  and  $\mathbf{b}$ . (a) A properly scaled problem, where  $\mathbf{A}$  and  $\mathbf{b}$  have the same norm. (b) The norms of  $\mathbf{A}$  and  $\mathbf{b}$  differ by a factor of four.

The second point is that the method implicitly assumes that the relative errors associated with the data matrix  $\mathbf{A}$



and observation vector  $\mathbf{b}$  are comparable. A large error in either input matrix will skew the TLS solution relative to the pattern realized in nature.

An accurate and reliable estimation of  $\mathbf{E}$  and  $\mathbf{r}$  are paramount to the TLS solution. The value of the correction,  $[\mathbf{E}|\mathbf{r}]$ , tells us how far to move or perturb the space of  $[\mathbf{A}|\mathbf{b}]$  to obtain the solution  $\mathbf{x}$ . This is accomplished via the Singular Value Decomposition (SVD).

This process begins with the augmentation of the data matrix  $\mathbf{A}$  with the observation vector  $\mathbf{b}$  giving a new matrix  $\mathbf{C}=[\mathbf{A}|\mathbf{b}]$ . The matrix  $\mathbf{C}$  is factored into three distinct components orthonormal matrices  $\mathbf{U}$  and  $\mathbf{V}$  and a diagonal matrix  $\mathbf{\Sigma}$ .

$$\mathbf{C}=[\mathbf{A}|\mathbf{b}]=\mathbf{U}\mathbf{\Sigma}\mathbf{V}^T \quad (22)$$

$$=\begin{pmatrix} \mathbf{u}^{(1)} & \mathbf{u}^{(2)} & \dots & \mathbf{u}^{(n+1)} \end{pmatrix} \begin{pmatrix} \sigma_1 & 0 & \dots & 0 \\ 0 & \sigma_2 & \dots & 0 \\ \vdots & \vdots & \ddots & \vdots \\ 0 & 0 & \dots & \sigma_n \end{pmatrix} \begin{pmatrix} \mathbf{v}^{(1)T} \\ \mathbf{v}^{(2)T} \\ \vdots \\ \mathbf{v}^{(n+1)T} \end{pmatrix} \quad (23)$$

$$=\sigma_1 \mathbf{u}^{(1)} \mathbf{v}^{(1)T} + \sigma_2 \mathbf{u}^{(2)} \mathbf{v}^{(2)T} + \dots + \sigma_n \mathbf{u}^{(n+1)} \mathbf{v}^{(n+1)T} \quad (24)$$

Equations (22), (23), and (24) are three formulations of the SVD. The result is a series (24) where the first term represents the largest singular value of the data, an analogue to the largest amount of energy, and the last term represents the least amount of energy in the system. This is very similar to Fourier series where the terms are multiple harmonics from lower frequencies to higher frequencies. SVD simply goes from higher energy to lower energy.

An important distinction of SVD is related to the ordering of the coefficients  $\sigma_i$ . The magnitude of each value of  $\sigma_i$  decreases with  $i$ , and therefore the most energy in the system is contained in the first component and the least energy is contained in the last component of the system.

As noted before the TLS solution corresponds to the correction  $\min_{\mathbf{b}+\mathbf{r} \in \mathbf{R}^{(A+E)}} \|\mathbf{E}|\mathbf{r}\|_F$  where  $\|\bullet\|_F$  denotes the Frobenius norm. Given the SVD, the Frobenius norm can be easily calculated.

$$\|\bullet\|_F = \sqrt{\sigma_1^2 + \sigma_2^2 + \dots + \sigma_n^2} \quad (25)$$

The Frobenius norm (25) differs greatly from the 2-norm used in the Ordinary Least Squares calculation. Recall, the solution to the Least Squares problem,  $\min_{\mathbf{x} \in R^n} \|\mathbf{Ax} - \mathbf{b}\|_2 = \min_{\mathbf{x} \in R^n} \|\mathbf{r}\|_2$ , where,  $\|\mathbf{C}\|_2 = \sigma_1$ . The 2-norm only considers the singular value with the highest energy ( $\sigma_1$ ), whereas, the Frobenius norm considers a range of singular values. Thus, the Frobenius norm contains a more inclusive representation of the system.

$$\tilde{\mathbf{C}} = \sigma_1 \mathbf{u}^{(1)} \mathbf{v}^{(1)T} + \sigma_2 \mathbf{u}^{(2)} \mathbf{v}^{(2)T} + \dots + \sigma_n \mathbf{u}^{(n)} \mathbf{v}^{(n)T} \quad (26)$$

$$\mathbf{\Delta} = -\sigma_{n+1} \mathbf{u}^{(n+1)} \mathbf{v}^{(n+1)T} = -\mathbf{C} \mathbf{v}^{(n+1)} \mathbf{v}^{(n+1)T} \quad (27)$$

$$\sigma_{n+1} = \min_{\text{rank}(\mathbf{C}+\mathbf{\Delta}) < n+1} \|\mathbf{\Delta}\|_F \quad (28)$$

Given (24), the closest (in a  $\|\bullet\|_F$  sense) rank  $n$   $\tilde{\mathbf{C}}$  to  $\mathbf{C}$  is given by (26), which is simply (24) with the last term dropped. Therefore (27) and (28) are true.

$$[\mathbf{A}+\mathbf{E}|\mathbf{b}+\mathbf{r}]\begin{bmatrix} \mathbf{x} \\ -1 \end{bmatrix}=0 \quad (29)$$

Consider  $\mathbf{C}=[\mathbf{A}|\mathbf{b}]$ , which has rank  $(n+1)$ .  $\mathbf{A}$  is rank  $n$  and when augmented with  $\mathbf{b}$  the rank becomes  $(n+1)$ . The TLS problem can be reformulated as (29), which implies that  $\tilde{\mathbf{C}}=[\mathbf{A}+\mathbf{E}|\mathbf{b}+\mathbf{r}]$  is no more than rank  $n$ , because  $\tilde{\mathbf{C}}$  is equal to  $\mathbf{C}$  with the last term removed. The last term in  $\mathbf{C}$  is used to formulate the correction matrix  $\Delta$ .

Ultimately, what is sought is a matrix  $\Delta=[\mathbf{E}|\mathbf{r}]\in R^{m \times (n+1)}$  that describes the minimum perturbation to the data matrix  $\mathbf{A}$ , and the observation vector  $\mathbf{b}$  such that  $\tilde{\mathbf{C}}$  is rank  $n$  and the solution for (29) exists.

It follows that the solution can be determined via the last  $(n+1)$  column of  $\mathbf{v}$ , defined as  $\mathbf{v}^{(n+1)}=\begin{bmatrix} \mathbf{y} \\ \alpha \end{bmatrix}$ , where  $\mathbf{y}\in\mathbf{R}^n$ , and  $\alpha\neq 0$ . If  $\mathbf{x}=-[\mathbf{y}/\alpha]$ , and  $\Delta=[\mathbf{E}|\mathbf{r}]=-\mathbf{C}\mathbf{v}\mathbf{v}^T$  then (29) is solved exactly.

### C. SCALING THE MATRIX

Ensuring that each equation is treated with equal value in the model requires that we normalize each row. This has two purposes: one is to prevent the appearance of spurious solutions, and the other is to up weight the more reliable equations (Lee, 1991). In this study, we divide each row by its Frobenius norm (for vectors the Frobenius norm is equivalent to the 2-norm), so that all of the equations have the same norm in the system.

It is sensible to presume that the continuity equation is less prone to error than either tracer equation, since there are no tracer values in continuity. For this reason, we multiplied the continuity equation by 10, effectively stating that continuity is more reliable than the other two. The value of the multiplier is important, but choosing 10 or 100 ultimately does not change the outcome. We simply give continuity a higher weight (relative importance to the problem) than the tracer equations.

#### D. PARAMETERIZATIONS OF THE VERTICAL FLUXES

Four models are discussed in this work, each having a different formulation of the fluxes ( $F_S$ ,  $F_T$ ).

$$F_T = K_T \frac{\partial T}{\partial z} \quad (30)$$

$$\alpha F_T = C(R_\rho)(\alpha \Delta T)^{4/3} \quad (31)$$

$$\alpha F_T = B C(R_\rho)(\alpha \Delta T)^{4/3} \quad (32)$$

Equation (30) is the classical form of flux that is dependent on the gradient of the tracer (temperature or salinity). This form is explored in both a one-dimensional model and a three-dimensional model.

Equations (31) and (32) are based on Turner's 4/3 flux law and invokes a more specific formulation proposed by Kelley (1990). Equation (31) is explored where the formulation of  $C(R_\rho)$  is unknown, while (32) has the full form of  $C(R_\rho)$  and the amplitude is unknown.

In Chapter IV, we present the one-dimensional model, which corresponds to the (30) formulation of the fluxes, and the three three-dimensional models: Model 1, Model 2, and

Model 3, which correspond to the flux formulations in equations (30), (31), and (32), respectively.

Recall, the solution vector  $\mathbf{x} \in R^n$  is composed of  $n$  elements that represent the unknowns  $(u, v, w, F_s, F_T)$  in the discretized model. Each element in  $\mathbf{x}$  must be multiplied by  $x_r$  to recover the correct value of the unknown. The output of the model is the vector  $\mathbf{x}$ .

## IV. MODEL RESULTS

The previous chapters described the framework necessary to implement the model. In this chapter, the results of the four different models are presented. As discussed in Chapter III, some of the elements of the model framework are adjusted to better understand the physical processes at work in the diffusive staircases. Each model will be described independently.

### A. ONE-DIMENSIONAL MODEL

The one-dimensional model was developed as a precursor to the larger, more dynamically inclusive three-dimensional model. The one-dimensional model allowed us to understand how the model worked and what type of output to expect. It also allowed us to observe the role of horizontal advection in the flux calculations.

$$\begin{aligned} & \frac{2(h_{k+1}T_0 + h_0C_{k+1})}{h_0 + h_{k+1}} w_{k+\frac{1}{2}} - \frac{2(h_0T_{k-1} + h_{k-1}T_0)}{h_{k-1} + h_0} w_{k-\frac{1}{2}} \\ & + \frac{4(T_0 - S_{k+1})}{h_0 + h_{k+1}} K_{T_{k+\frac{1}{2}}} - \frac{4(T_{k-1} - T_0)}{h_{k-1} + h_0} K_{T_{k-\frac{1}{2}}} = 0 \end{aligned} \quad (33)$$

$$\begin{aligned} & \frac{2(h_{k+1}S_0 + h_0S_{k+1})}{h_0 + h_{k+1}} w_{k+\frac{1}{2}} - \frac{2(h_0S_{k-1} + h_{k-1}S_0)}{h_{k-1} + h_0} w_{k-\frac{1}{2}} \\ & + \frac{4(S_0 - S_{k+1})}{h_0 + h_{k+1}} K_{S_{k+\frac{1}{2}}} - \frac{4(S_{k-1} - S_0)}{h_{k-1} + h_0} K_{S_{k-\frac{1}{2}}} = 0 \end{aligned} \quad (34)$$

$$w_{k-\frac{1}{2}} - w_{k+\frac{1}{2}} = 0 \quad (35)$$

In this case, we neglect all horizontal velocity components and consider a system where vertical advection of salt and heat are balanced by diffusion. Equations (33), (34) and (35) are used for the inverse one-dimensional calculation. Depth is measured from the sea surface and therefore vertical velocity is positive downward.

Layer	Potential Temperature (degC)	Salinity (PSU)	Layer Thickness (m)	Layer Depth
1	-0.6533	34.3128	1.7605	220.5104
2	-0.6065	34.3307	1.9772	222.3872
3	-0.5589	34.3484	1.9700	224.4895
4	-0.5080	34.3654	2.0280	226.6684
5	-0.4513	34.3847	2.1539	229.5241
6	-0.4074	34.4006	2.1856	232.3383
7	-0.3687	34.4140	2.2638	234.2862
8	-0.3484	34.4243	1.1092	237.7177
9	-0.3084	34.4338	1.8727	239.5300
10	-0.2530	34.4521	2.7462	240.8740
11	-0.1792	34.4767	2.4911	245.2952
12	-0.1191	34.4967	3.2346	249.0272
13	-0.0747	34.5121	2.8019	252.1884
14	-0.0334	34.5261	2.2499	254.8196
15	0.0062	34.5380	2.3186	257.1105
16	0.0449	34.5506	2.3997	259.7826
17	0.0866	34.5641	3.5397	262.5461
18	0.1358	34.5825	2.3701	265.8477
19	0.1705	34.5953	2.8645	267.9215

Table 4. One dimensional data set consisting of average values of potential temperature, salinity, and layer thickness for the entire basin.

The inputs into the one-dimensional inverse model are average values of potential temperature, salinity and layer thickness. The total set of 3452 profiles is used to obtain averages. These data are shown in Table 4. It is clear that temperature and salinity increase with depth, while the layer thickness ranges from just over 1 meter to just over 3

meters. The average thickness is approximately 2.33 meters. The average change in temperature between layers is approximately 0.046°C, and the average change in salinity between layers is approximately 0.16 PSU.

Model parameters ( $w$ ,  $K_T$ ,  $K_S$ ) were calculated for each interface above and below layers 2 thru 18. Layers 1 and 19 are used for input on the boundaries only. Thus 18 values of the unknowns are calculated. Vertical velocity ( $w$ ) is found to be constant, which is consistent with the integrated form of the continuity equation. As expected, heat Flux ( $F_H$ ) is upward (positive), and  $K_T$  is negative.

Interface	Fh(W/m <sup>2</sup> )	Kt(10 <sup>-5</sup> m <sup>2</sup> s <sup>-1</sup> )	w(10 <sup>-7</sup> m/s)	Rrho
1	0.84	-0.85	-5	6.23
2	0.88	-0.98	-5	5.97
3	0.95	-1.03	-5	5.29
4	0.84	-1.06	-5	5.30
5	0.96	-1.55	-5	5.54
6	1.51	-1.93	-5	5.23
7	0.68	-2.90	-5	7.57
8	1.18	-1.35	-5	3.50
9	2.62	-1.61	-5	4.82
10	0.99	-1.50	-5	4.80
<b>Mean</b>	<b>1.56</b>	<b>-2.31</b>	<b>-5.00</b>	<b>5.04</b>

Table 5. One-dimensional Model 1 results.

Table 5 is the results from the first one dimensional model run. The most important output for this model is the Heat Flux ( $F_H$ ). The mean heat flux in the upward direction is 1.56 W/m<sup>2</sup>. This is a critical value to determining whether diffusive convection contributes to ice melt.

The second result is the calculated value of the amplitude of  $C(R_\rho)$ . This value is 0.0032 in the Kelley



(1990) formulation of the 4/3 flux law (8). Recall that this formulation was derived using laboratory experiments that may not represent what is observed in nature. We attempt to calibrate this formulation to best represent the Arctic data.

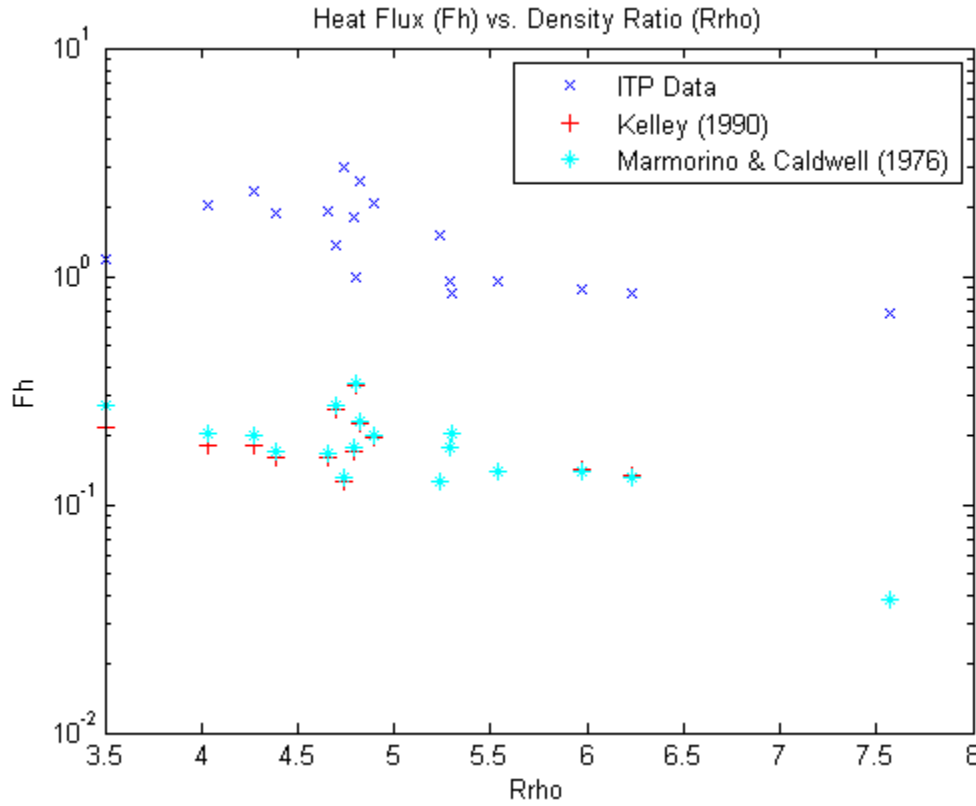


Figure 15. Comparison of the two laboratory representations of Heat Flux and the calculated value of Heat Flux from the one-dimensional Model 1.

Figure 15 illustrates that the heat flux ( $F_h$ ) calculated in one-dimensional Model 1 is roughly an order of magnitude larger for the Arctic data.

$$F_h = -K_t \frac{\Delta T}{\Delta Z} \quad (36)$$

The heat flux was calculated using (36). Where  $\Delta T$  represents the temperature change between the layer above

and layer below the interface, and  $\Delta Z$  represents the distance between the centers of the two layers.

<b>Interface</b>	<b>Fh (Model)</b>	<b>Fh (Kelley)</b>
1	0.84	0.13
2	0.88	0.14
3	0.95	0.18
4	0.84	0.20
5	0.96	0.14
6	1.51	0.13
7	0.68	0.04
8	1.18	0.22
9	2.62	0.22
10	0.99	0.33
<b>Mean</b>	<b>1.56</b>	<b>0.18</b>

Table 6. Comparison of heat flux calculated using the one dimensional Model 1 and using Kelley (1990) formulation of the 4/3 flux law.

In this formulation of the heat flux, the magnitude of the flux is not only dependent on the change in temperature between the two layers, but also on the size of the two layers. This proposition is very different from the 4/3 flux law, which states that the heat flux is independent of depth or layer thickness. Comparison with the earlier calculations (Kelley, 1990) reveals an order of magnitude difference in heat fluxes seen in Table 6.

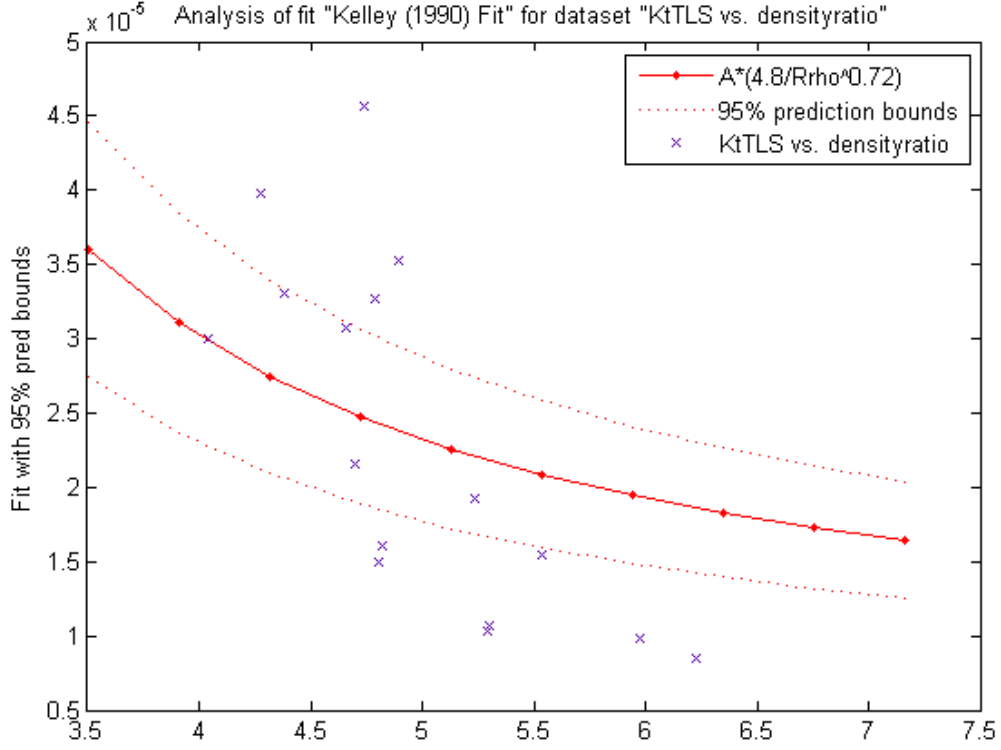


Figure 16. Fit of  $C(R_\rho)$  as proposed by Kelley (1990) to the one dimensional Model 1 results.

Figure 16 represents an attempt to calibrate the Kelley (1990) model to fit the fluxes obtained with the inverse model. This resulted in a calculation of the amplitude of  $C(R_\rho)$  based on the output of the curve fitting routine. The result is a value of the amplitude of  $C(R_\rho) = 0.0479$ , an order of magnitude larger than the amplitude of  $C(R_\rho)$  in the Kelley (1990) formulation. The upper and lower bounds, at the 95% confidence level, are 0.0603 and 0.0354 respectively. The associated RMSE is 0.0119, and the sum of the squared errors is  $2.4484e-005$ .

The one-dimensional case suggests that the 4/3 flux laws as stated by Kelley (1990) and Marmorino and Caldwell

(1976) are not applicable to the Arctic diffusive staircases in their original form. Instead an order of magnitude adjustment must be made to the equations that correspond to a new value of  $C(R_\rho)$ . This is similar to the idea of a transfer function proposed by Wilson (2007). Additionally, the curve is not a perfect fit to the data. Only five of the data points lie within the 95% confidence interval. There is a much steeper trend associated with this data that suggests an even stronger dependence on density ratio. The three dimensional model is more inclusive, and shows a trend more consistent with the laboratory results.

## **B. THREE-DIMENSIONAL MODEL**

### **1. Depth Dependent Discretization**

Model 1 utilizes the full three-dimensional discretization of the equations described by Lee and Veronis (1990). The three dimensional data set described in Chapter II is used as input to the model. The data set has 425 individual grid cells for which the model parameters will be calculated, resulting in a total of 1275 equations and 1073 unknowns. The critical values of parameters ( $w$ ,  $K_S$ ,  $K_T$ ) remain the same as the one dimensional dataset in that they are assumed to be constant at each interface. The model calculated  $u$  and  $v$  components of velocity as well.

Interface	Fh(W/m <sup>2</sup> )	Kt(10 <sup>-5</sup> m <sup>2</sup> s <sup>-1</sup> )	w(10 <sup>-7</sup> m/s)	Rrho
1	2.15	3.02	5.00	6.36
2	2.29	2.95	-5.88	6.07
3	2.41	2.76	-13.58	5.29
4	1.54	2.17	-35.91	5.50
5	1.73	2.69	-18.59	5.66
6	1.70	3.17	-23.94	5.44
7	3.33	2.92	9.82	5.52
8	1.36	1.88	-1.67	4.34
9	2.27	3.01	29.37	4.33
10	1.91	2.88	-6.84	4.75
<b>Mean</b>	<b>2.07</b>	<b>2.74</b>	<b>-6.22</b>	<b>5.32</b>

Table 7. Three dimensional Model 1 results.

Table 7 is the results of three-dimensional model 1. The heat flux ( $F_h$ ) is consistent with that of the one dimensional model for interfaces 1 through 10. Below interface 10 the heat fluxes begin to rise to questionable levels. The mean heat flux  $-2.07 \text{ W/m}^2$  is for the first 10 interfaces. The assumption of uniform velocity at the interface resulted in vastly different values of vertical velocity throughout the data.

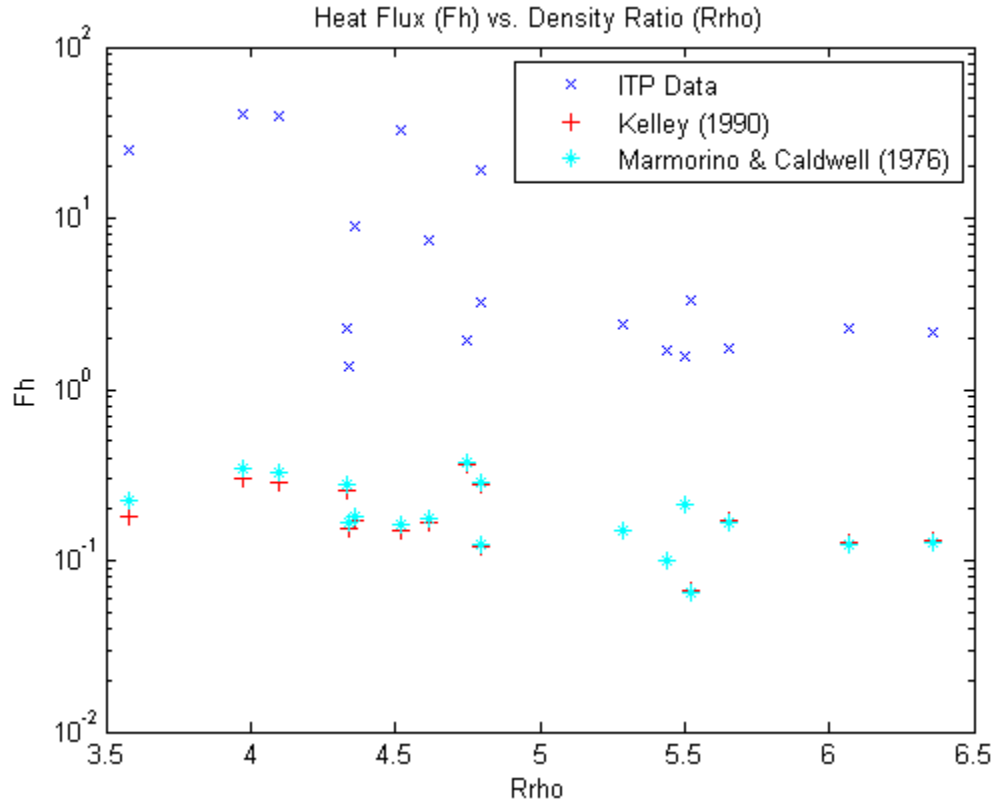


Figure 17. Comparison of the two laboratory representations of Heat Flux and the calculated value of Heat Flux from the three-dimensional Model 1.

As in the one dimensional model it is important to show how these results relate to the 4/3 flux laws. Figure 17 is a plot of the calculated values for heat flux and those using the laboratory derived formulations. Like the one dimensional model calculations, the three-dimensional model values of heat flux are about an order of magnitude larger than those calculated using the laboratory formulations of the 4/3 flux law.

<b>Interface</b>	<b>Fh (Model)</b>	<b>Fh (Kelley)</b>
1	2.15	0.13
2	2.29	0.13
3	2.41	0.15
4	1.54	0.21
5	1.73	0.17
6	1.70	0.10
7	3.33	0.07
8	1.36	0.16
9	2.27	0.26
10	1.91	0.36
<b>Mean</b>	<b>2.07</b>	<b>0.19</b>

Table 8. Comparison of heat flux calculated using the three-dimensional Model 1 and the Kelley (1990) formulation of the 4/3 flux law.

The heat fluxes associated with these values of diffusivity are naturally an order of magnitude larger than those calculated using the Kelley (1990) formulation. Table 8 is a comparison of heat flux calculations. The heat flux from the model is calculated using (36). The mean value shown for the model calculation is the mean for just the first 10 interfaces. The mean for the Kelley formulation is that of all 19 interfaces. The difference between the two is a full order of magnitude.

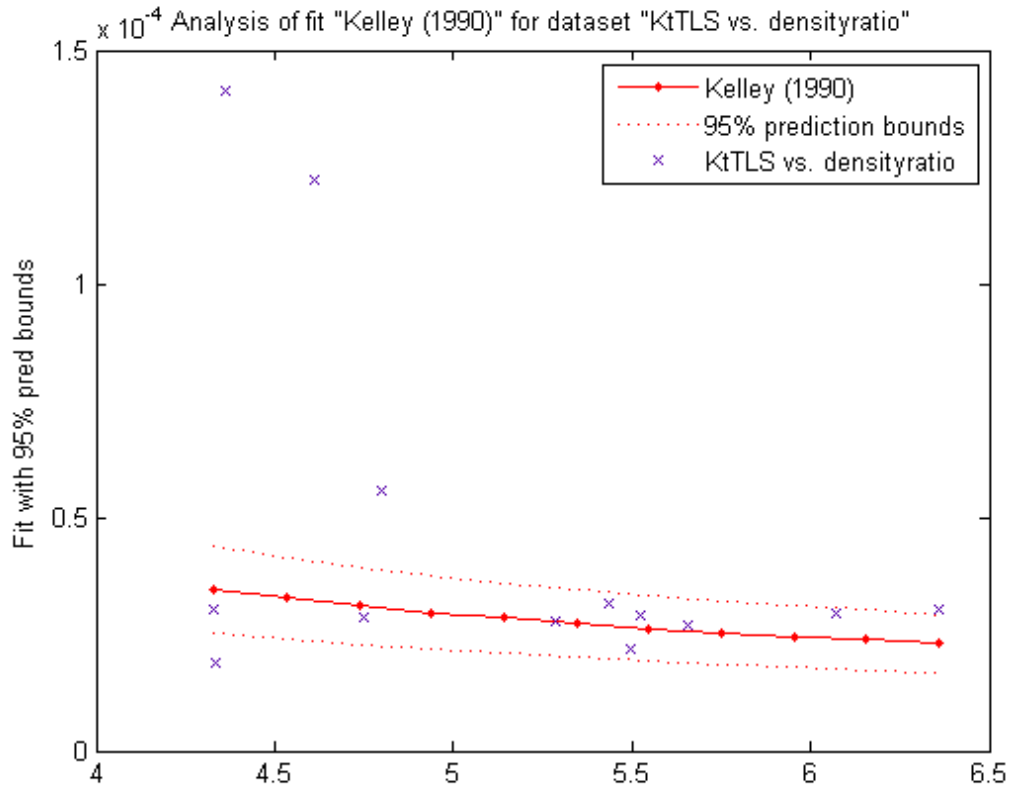


Figure 18. Fit of  $C(R_\rho)$  as proposed by Kelley (1990) to the three dimensional model 1 results.

Figure 18 is the attempt to calibrate the 4/3 flux law. The fit curve excludes the interfaces 14-18 since the results for those interfaces were extremely far from the rest of the data. The results of the curve fitting were a value of the amplitude of  $C(R_\rho) = 0.0635$ . The upper and lower bounds of the 95% confidence interval are 0.0805 and 0.0464 respectively. Nearly all of the data points fall within these bounds, which shows that the general trend in the data is similar to that of Kelley (1990), yet the model results are an order of magnitude larger.



## 2. 4/3 Flux Law Discretization with $C(R_\rho)$ Unknown

In order to compare the results of the previous section to the 4/3 flux law more directly, the model discretization had to be changed. The new model discretization corresponds to three-dimensional Model 2 as discussed in Chapter III, Section D.

$$\begin{aligned}
& \frac{(T_0 + T_{i+1})(h_0 + h_{i+1})}{2l_x} u_{i+\frac{1}{2}} - \frac{(T_{i-1} + T_0)(h_{i-1} + h_0)}{2l_x} u_{i-\frac{1}{2}} \\
& + \frac{(T_0 + T_{j+1})(h_0 + h_{j+1})}{2l_y} v_{j+\frac{1}{2}} - \frac{(T_{j-1} + T_0)(h_{j-1} + h_0)}{2l_y} v_{j-\frac{1}{2}} \\
& + \frac{2(h_{k+1}T_0 + h_0T_{k+1})}{h_0 + h_{k+1}} w_{k+\frac{1}{2}} - \frac{2(h_0T_{k-1} + h_{k-1}T_0)}{h_{k-1} + h_0} w_{k-\frac{1}{2}} \\
& + \frac{4|(T_0 - T_{k+1})|^{\frac{4}{3}}}{2h(\overline{\Delta T})^{\frac{1}{3}}} C(R_\rho)_{k+\frac{1}{2}} - \frac{4|(T_{k-1} - T_0)|^{\frac{4}{3}}}{2h(\overline{\Delta T})^{\frac{1}{3}}} C(R_\rho)_{k-\frac{1}{2}} = 0
\end{aligned} \tag{37}$$

$$\begin{aligned}
& \frac{(S_0 + S_{i+1})(h_0 + h_{i+1})}{2l_x} u_{i+\frac{1}{2}} - \frac{(S_{i-1} + S_0)(h_{i-1} + h_0)}{2l_x} u_{i-\frac{1}{2}} \\
& + \frac{(S_0 + S_{j+1})(h_0 + h_{j+1})}{2l_y} v_{j+\frac{1}{2}} - \frac{(S_{j-1} + S_0)(h_{j-1} + h_0)}{2l_y} v_{j-\frac{1}{2}} \\
& + \frac{2(h_{k+1}S_0 + h_0S_{k+1})}{h_0 + h_{k+1}} w_{k+\frac{1}{2}} - \frac{2(h_0S_{k-1} + h_{k-1}S_0)}{h_{k-1} + h_0} w_{k-\frac{1}{2}} \\
& + \frac{4|(S_0 - S_{k+1})|^{\frac{4}{3}}}{2h(\overline{\Delta S})^{\frac{1}{3}}} C(R_\rho)_{k+\frac{1}{2}} - \frac{4|(S_{k-1} - S_0)|^{\frac{4}{3}}}{2h(\overline{\Delta S})^{\frac{1}{3}}} C(R_\rho)_{k-\frac{1}{2}} = 0
\end{aligned} \tag{38}$$

The equations remain the same except for the last two terms. The coefficients of diffusivity are changed to reflect the  $(\Delta T)^{4/3}$  relationship described by Turner (1973). This relationship is normalized by the mean layer thickness and mean temperature gradient in order to maintain the same

dimensionality as the original discretization. The continuity equation remained the same. The data set, number of equations, and number of unknowns are the same as the previous section.

$$F_T = \frac{2 \left( C(R_\rho) (\Delta T)^{\frac{4}{3}} \right)}{2\bar{h}(\overline{\Delta T})^{\frac{1}{3}}} \quad (39)$$

$$F_S = \frac{2 \left( C(R_\rho) (\Delta S)^{\frac{4}{3}} \right)}{2\bar{h}(\overline{\Delta S})^{\frac{1}{3}}} \quad (40)$$

The equations used to calculate the fluxes are different because of the changes to the discretization. Temperature (39) and salinity (40) fluxes are now a function of  $(\Delta T)^{4/3}$ , and the fluxes must be normalized by the mean layer thickness and mean temperature gradient as well.

Interface	Fh(W/m^2)	Kt(10^-5 m2s^-1)	w(10^-7 m/s)	Rrho
1	0.69	0.78	5.00	6.36
2	0.79	0.98	-12.14	6.07
3	0.86	1.04	3.74	5.29
4	0.73	0.60	8.01	5.50
5	0.72	0.73	-0.90	5.66
6	0.53	0.96	13.52	5.44
7	0.45	1.19	-1.68	5.52
8	0.56	0.83	3.99	4.34
9	0.82	0.74	-8.36	4.33
10	0.85	0.50	2.47	4.75
<b>Mean</b>	<b>-9.96</b>	<b>-0.83</b>	<b>1.37</b>	<b>5.32</b>

Table 9. Three-dimensional Model 2 results.

The model results are presented in Table 9. We again observe questionable heat fluxes below layer 10, which we attribute to uncertainties of clearly identifying layers 11-

15. Those results are not shown. Overall the heat fluxes are less than 1 W/m<sup>2</sup>. The mean heat flux in the upper 10 layers is 0.70 W/m<sup>2</sup>.

Interface	Fh (Model)	Fh (Kelley)
1	0.69	0.13
2	0.79	0.13
3	0.86	0.15
4	0.73	0.21
5	0.72	0.17
6	0.53	0.10
7	0.45	0.07
8	0.56	0.16
9	0.82	0.26
10	0.85	0.36
<b>Mean</b>	<b>0.70</b>	<b>0.19</b>

Table 10. Comparison of heat flux calculated using the three-dimensional model 2 and the Kelley (1990) formulation of the 4/3 flux law.

Table 10 shows that the fluxes in this inverse calculation are a factor of 3-5 larger than the Kelley (1990) calculation. While they are not a full order of magnitude different as in the previous section, there is still a significant difference.

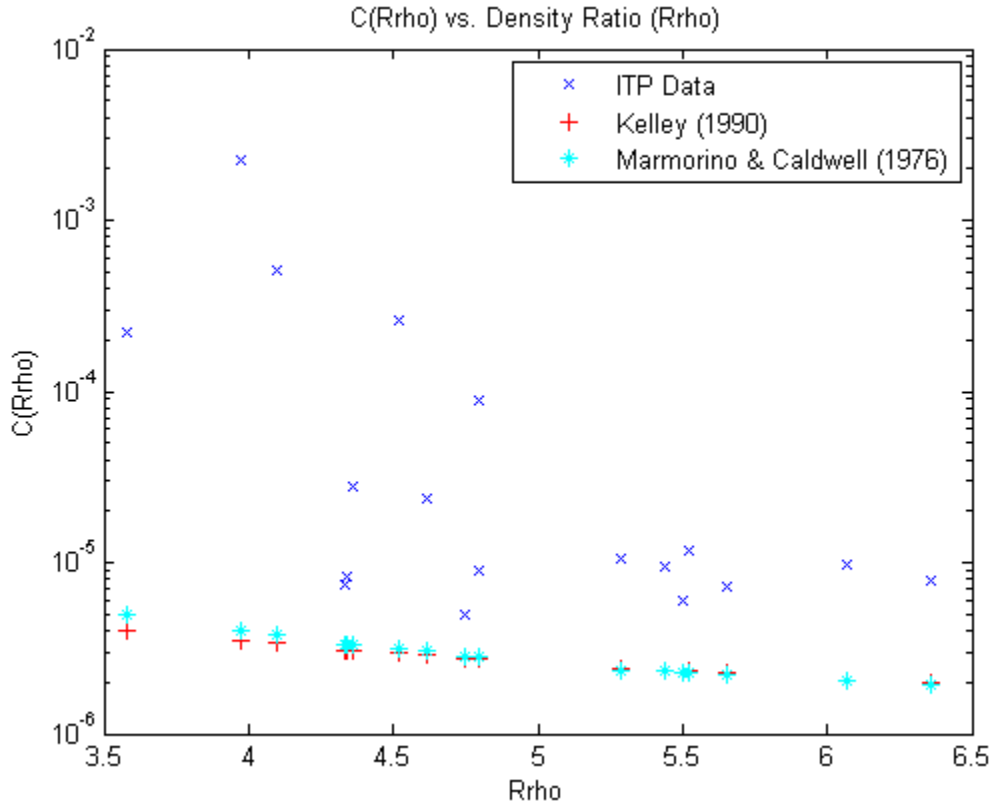


Figure 19. Comparison of the two laboratory representations of  $C(R_\rho)$  and the calculated value of  $C(R_\rho)$  from the three-dimensional Model 2.

Figure 19 is the  $C(R_\rho)$  plot. The general pattern of the diffusivities calculated by the inverse model is the same. However, the difference between the model and the Kelley (1990) and Marmorino and Caldwell (1976) calculations is only a factor of 3-5. The five outliers for lower values of density ratio correspond to the lower five layers, which show anomalous results.

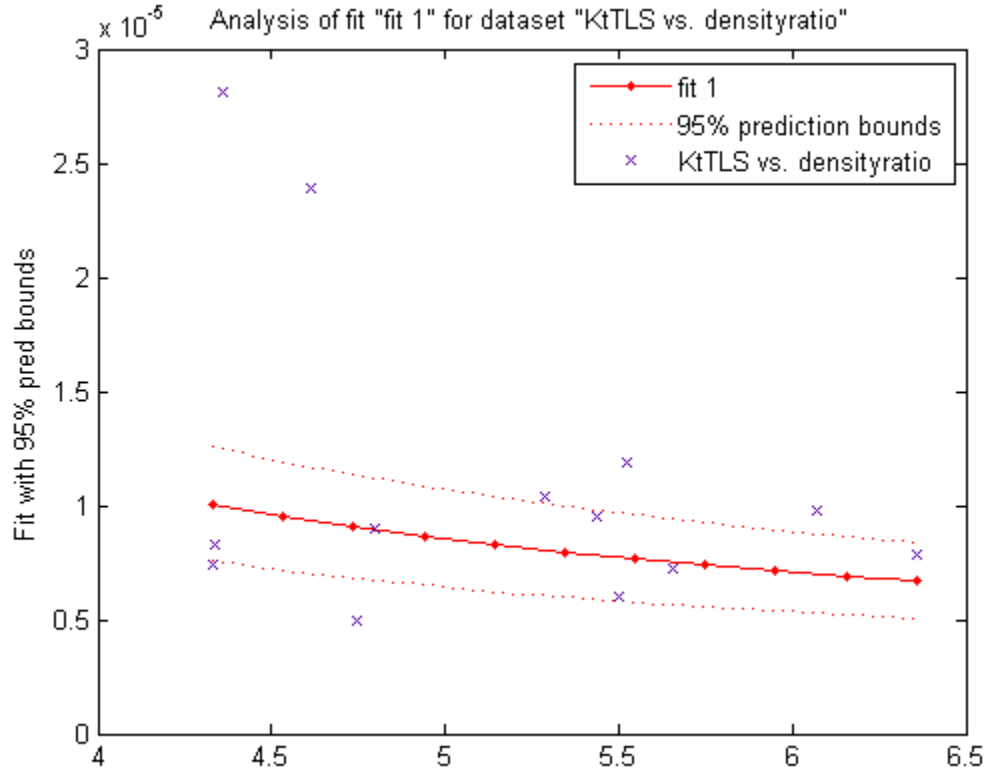


Figure 20. Fit of  $C(R_\rho)$  as proposed by Kelley (1990) to the three-dimensional Model 2 results.

Removing the lower five layers from the curve fitting routine allows for a much better estimation of the amplitude of  $C(R_\rho)$ . Figure 20 is the result of the curve fitting routine. The result is a value of the amplitude of  $C(R_\rho) = 0.0185$ . The upper and lower bounds are equal to 0.0232 and 0.0139 respectively. This represents a significantly reduced confidence interval compared to Model 1.

### 3. $C(R_\rho)$ Calculation using Kelley (1990) 4/3 Flux Law

Now we attempt to directly extract the amplitude of the coefficient  $C(R_\rho)$  from the inverse calculation. The entire Kelley (1990) formulation of the 4/3 flux law is used as the

coefficient in the model. Thus, the result is an exact value for the amplitude of  $C(R_\rho)$  as model output. We assume that the pattern of  $C(R_\rho)$  is correctly captured by the laboratory experiments, but the amplitude (B) requires calibration.

$$\begin{aligned}
& \frac{(T_0 + T_{i+1})(h_0 + h_{i+1})}{2l_x} u_{i+\frac{1}{2}} - \frac{(T_{i-1} + T_0)(h_{i-1} + h_0)}{2l_x} u_{i-\frac{1}{2}} \\
& + \frac{(T_0 + T_{j+1})(h_0 + h_{j+1})}{2l_y} v_{j+\frac{1}{2}} - \frac{(T_{j-1} + T_0)(h_{j-1} + h_0)}{2l_y} v_{j-\frac{1}{2}} \\
& + \frac{2(h_{k+1}T_0 + h_0T_{k+1})}{h_0 + h_{k+1}} w_{k+\frac{1}{2}} - \frac{2(h_0T_{k-1} + h_{k-1}T_0)}{h_{k-1} + h_0} w_{k-\frac{1}{2}} \\
& + B \frac{4 \left( \left( \frac{\alpha g \kappa}{\text{Pr}} \right)^{\frac{1}{3}} \exp \left( \frac{4.8}{R_\rho^{0.72}} \right) |T_0 - T_{k+1}|^{\frac{4}{3}} \right)}{2h(\overline{\Delta T})^{\frac{1}{3}}} \\
& - B \frac{4 \left( \left( \frac{\alpha g \kappa}{\text{Pr}} \right)^{\frac{1}{3}} \exp \left( \frac{4.8}{R_\rho^{0.72}} \right) |T_{k-1} - T_0|^{\frac{4}{3}} \right)}{2h(\overline{\Delta T})^{\frac{1}{3}}} = 0
\end{aligned} \tag{41}$$

$$\begin{aligned}
& \frac{(S_0 + S_{i+1})(h_0 + h_{i+1})}{2l_x} u_{i+\frac{1}{2}} - \frac{(S_{i-1} + S_0)(h_{i-1} + h_0)}{2l_x} u_{i-\frac{1}{2}} \\
& + \frac{(S_0 + S_{j+1})(h_0 + h_{j+1})}{2l_y} v_{j+\frac{1}{2}} - \frac{(S_{j-1} + S_0)(h_{j-1} + h_0)}{2l_y} v_{j-\frac{1}{2}} \\
& + \frac{2(h_{k+1}S_0 + h_0S_{k+1})}{h_0 + h_{k+1}} w_{k+\frac{1}{2}} - \frac{2(h_0S_{k-1} + h_{k-1}S_0)}{h_{k-1} + h_0} w_{k-\frac{1}{2}} \\
& + B \frac{4 \left( \left( \frac{\alpha g \kappa}{\text{Pr}} \right)^{\frac{1}{3}} \exp \left( \frac{4.8}{R_\rho^{0.72}} \right) |S_0 - S_{k+1}|^{\frac{4}{3}} \right)}{2h(\overline{\Delta S})^{\frac{1}{3}}} \\
& - B \frac{4 \left( \left( \frac{\alpha g \kappa}{\text{Pr}} \right)^{\frac{1}{3}} \exp \left( \frac{4.8}{R_\rho^{0.72}} \right) |S_{k-1} - S_0|^{\frac{4}{3}} \right)}{2h(\overline{\Delta S})^{\frac{1}{3}}} = 0
\end{aligned} \tag{42}$$

We also assume that B is constant and that it is not dependent on the density ratio, so in the model it is treated as a single unknown. This reduces the number of unknowns to 1038 with the number of equations remaining 1275. The last two terms are again normalized by the mean layer thickness and mean temperature gradient in order to maintain the same dimensionality as the original discretization. The continuity equation remained the same.

<b>Interface</b>	<b>Fh(W/m<sup>2</sup>)</b>	<b>w(10<sup>-7</sup> m/s)</b>	<b>Rrho</b>
1	0.49	5.00	6.36
2	0.47	-2.53	6.07
3	0.55	-5.07	5.29
4	0.79	11.88	5.50
5	0.63	-11.01	5.66
6	0.37	23.70	5.44
7	0.25	-43.40	5.52
8	0.58	91.44	4.34
9	0.96	-108.90	4.33
10	1.34	82.35	4.75
<b>Mean</b>	<b>0.64</b>	<b>4.35</b>	<b>5.32</b>

Table 11. Three-dimensional Model 3 results.

The results are shown in Table 11. The heat fluxes are generally below 1 W/m<sup>2</sup>, with the average heat flux being 0.70 W/m<sup>2</sup>. The difference is still significant, and is comparable to the three dimensional model 2 results. The vertical velocities are also anomalously high below layer 11.

<b>Interface</b>	<b>Fh (Model)</b>	<b>Fh (Kelley)</b>
1	0.49	0.13
2	0.47	0.13
3	0.55	0.15
4	0.79	0.21
5	0.63	0.17
6	0.37	0.10
7	0.25	0.07
8	0.58	0.16
9	0.96	0.26
10	1.34	0.36
<b>Mean</b>	<b>0.70</b>	<b>0.19</b>

Table 12. Comparison of heat flux calculated using the three-dimensional Model 3 and the Kelley (1990) formulation of the 4/3 flux law.



Table 12 is the comparison of Model 3 results and the fluxes calculated using the Kelley (1990) formulation of the 4/3 flux law. The difference between the two is exactly a factor of 3.717 throughout the data. This makes sense in that all we changed is the amplitude of the calculation, and thus all we changed is the multiplying factor determining the fluxes.

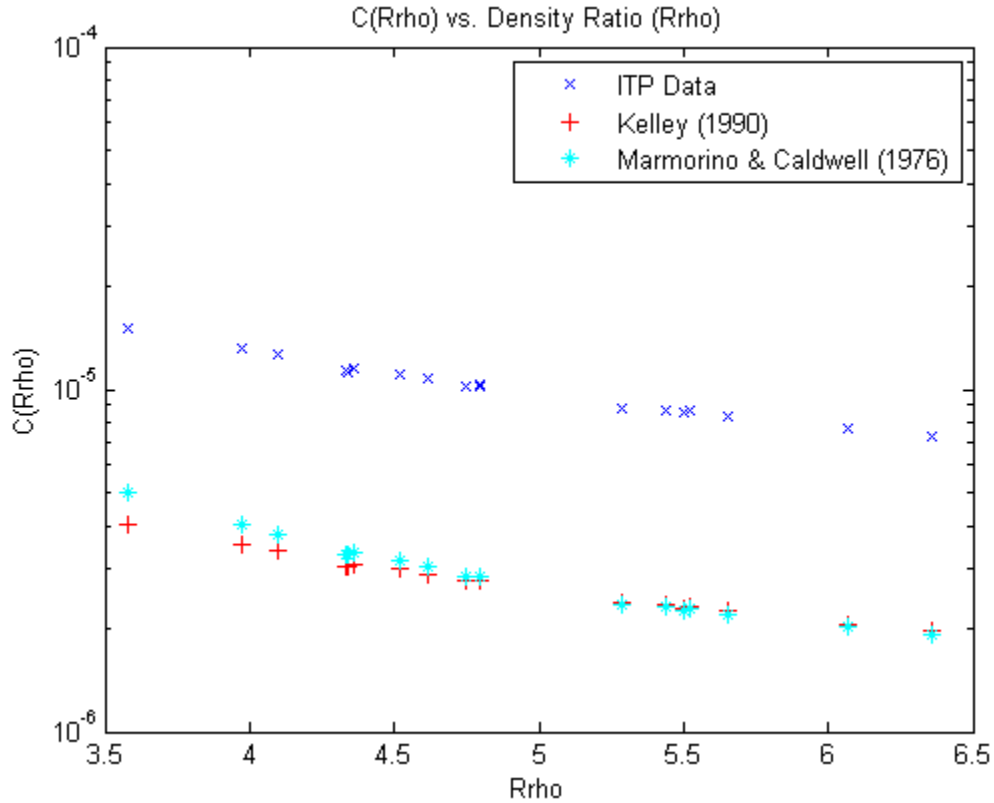


Figure 21. Comparison of the two laboratory representations of  $C(R_\rho)$  and the calculated value of  $C(R_\rho)$  from the three-dimensional Model 3.

Figure 21 is the plot of density ratio versus diffusivity. The trend in the calculated values from the inverse model is the same as the laboratory results. The difference in magnitude is approximately a factor of 3.

There are no anomalous results since the whole parameterization from Kelley (1990) was used.

The data fitting routine in this case is not necessary, since the output of the inverse calculation is a direct calculation of the coefficient  $C$ .

THIS PAGE INTENTIONALLY LEFT BLANK

## V. DISCUSSION AND CONCLUSIONS

### A. DISCUSSION

This work attempts to infer the vertical heat fluxes through diffusive staircases in the Beaufort Sea using techniques of inverse modeling. Table 13 summarizes the heat flux results for the four models presented in Chapter IV. The values of the fluxes are significantly higher than laboratory extrapolation (Kelley, 1990) would suggest. The mean fluxes shown are for the upper 10 layers in all of the models. The mean of those four is approximately  $1.25 \text{ W/m}^2$ . This suggests that the upward heat flux due to diffusive convection is sufficient enough to contribute to sea ice melt in the southern Beaufort Sea.

Interface	Fh (1D Model)	Fh (3D Model 1)	Fh (3D Model 2)	Fh (3D Model 3)	Fh (Kelley)
1	0.84	2.15	0.69	0.49	0.13
2	0.88	2.29	0.79	0.47	0.13
3	0.95	2.41	0.86	0.55	0.15
4	0.84	1.54	0.73	0.79	0.21
5	0.96	1.73	0.72	0.63	0.17
6	1.51	1.70	0.53	0.37	0.10
7	0.68	3.33	0.45	0.25	0.07
8	1.18	1.36	0.56	0.58	0.16
9	2.62	2.27	0.82	0.96	0.26
10	0.99	1.91	0.85	1.34	0.36
Mean	1.56	2.07	0.70	0.64	0.19

Table 13. Comparison of heat fluxes calculated from all models.

The most glaring discrepancies in the calculations are the abnormally large flux values below layer 10 in three-dimensional models 1 and 2. One reason for these large flux

values is the dependence on layer thickness in the model discretization.

Layer	Thickness (m)
1	1.78
2	1.59
3	1.54
4	1.80
5	2.12
6	2.24
7	1.90
8	1.14
9	1.56
10	2.38
11	2.45
12	3.22
13	2.27
14	2.67
15	1.99
16	3.36
17	1.72
18	2.91
19	1.53

Table 14. Mean layer thicknesses.

Table 14 is the average layer thicknesses for each layer. The deeper the layers the larger the thickness values become. There is a significant increase in layer thickness below layer 10. Layer thickness is in the denominator in the vertical terms. This increase in thickness effectively reduces the value of the coefficient in the discretized model and requires an increase in the calculated unknown. A discretization scheme that uses an average layer thickness may reduce this erroneous result.

The one-dimensional model performs well, and is less variable than three-dimensional Models 1 and 2, and its variability is comparable to three-dimensional Model 3.

Neglecting horizontal velocity likely dampened the effect of the layer thickness dependence in the flux calculations. Thus, there were no erroneous results in the deeper layers.

$$u_r = \frac{g}{\rho_0 f} \int_{z_0}^z \frac{\partial \rho}{\partial y} dz \quad (43)$$

$$v_r = -\frac{g}{\rho_0 f} \int_{z_0}^z \frac{\partial \rho}{\partial x} dz \quad (44)$$

The vertically integrated thermal wind equations state that horizontal velocities are balanced by horizontal pressure gradients. This implies that the direction and magnitude of the horizontal velocity is strictly controlled by the thickness differences between adjacent cells in the data. The direction of the flow is calculated to be in the direction of the thinner cell, and the magnitude is a result of the relative differences in thickness between the two cells.

Layer thickness is in the numerator in the horizontal terms, possibly lowering the value of horizontal velocity. It is likely that the combination of the sensitivity of the vertical heat flux calculations and the sensitivity of the horizontal velocity terms to the layer thickness contributed to the anomalies in the deeper layers in the two models were both were factors in the calculation.

Model	Amplitude of $C(R_p)$
1D Model	0.0479
3D Model 1	0.0635
3D Model 2	0.0185
3D Model 3	0.0119
Kelley	0.0032
Marmorino & Caldwell	0.0086

Table 15. Comparison of amplitudes of the 4/3 flux law coefficient  $C(R_p)$ .

Table 15 compares the results of each models output for the coefficient of amplitude of  $C(R_p)$ . As one may expect, the formulations of the inverse calculation that more closely represents the Kelley (1990) formulation of the 4/3 flux law (3D Model 2 and 3D Model 3) yielded results that were closer to Kelley's value of the amplitude. However, these results are still a factor of 4-6 larger than Kelley's laboratory results. The one-dimensional model and the three-dimensional Model 1 both used the layer thickness dependent version of the model formulation and yielded results more than a full order of magnitude greater. Caro (2009) found results similar to Model 2 and 3 via two-dimensional direct numerical simulation, and Wilson (2007) found results similar to the 1D model and 3D Model 1 analyzing the ITP data.

The accuracy of the calculations is not directly addressed. There are several questions associated with the accuracy of the calculations that need to be answered with further study. One very important measure of how well the TLS algorithm performs is the condition number. The condition number measures the sensitivity of the solution of the system of equations to errors in the data. A small ( $\sim 1$ )

value of the condition number indicates a well conditioned system, and thus a system that is not too prone to solution error. The larger the condition number, the more sensitive the solution is to errors in the system. The condition number of the data matrix **A** in the one dimensional model is 781 indicating that the system is quite sensitive to data errors. The addition of more equations and more unknowns to the problem only increases the sensitivity. The condition numbers for three-dimensional Models 1-3 are on the order of  $10^8$ .

## **B. CONCLUSIONS**

The inverse modeling technique was successful at calculating the heat flux in the southern Beaufort Sea. There are sensitivities associated with the models due to the differences in layer thickness. In the lower layers, where thickness is greater, there is greater potential for large flux values and small horizontal velocities due to the larger values of layer thickness. Ultimately, the upper 10 layers showed that the mean heat fluxes were  $1.25 \text{ W/m}^2$ , and therefore likely to contribute to sea ice melt.

The data suggest that the amplitude of the exponential form of  $C(R_p)$  is likely within the range of a factor of 4 to nearly an order of magnitude larger than laboratory results (Kelley, 1990; Marmorino & Caldwell, 1976) indicate. The application of the inverse model has shown that extrapolation of laboratory results to the ocean is not perfect, and in this case, not representative of observed ocean conditions. Laboratory experiments provide a foundation for which observational scientists can pose



hypotheses, but ultimately, the true test of a laboratory based theory is how well the observed data corroborates the results.

### **C. RECOMMENDATIONS**

Several questions remain unanswered. First, is there a way to improve the condition of the system of equations? Second, what is the spatial variability of the heat fluxes throughout the Beaufort Sea? Finally, can a well designed experiment, where data is collected systematically in a grid, improve the results?

It would be beneficial to add a set of equations to constrain velocities to known physical principles such as Thermal Wind or Conservation of Vorticity. Lee and Veronis (1990) did do this, and their results were more consistent than estimates based entirely on the advection-diffusion equations.

The spatial variability of the model must be explored. This study only used one location in the southern Beaufort Sea. The model needs to be run in several locations to gain a perspective on the changes in fluxes throughout the region.

The possibility of Inverse Modeling using an unstructured grid should be explored. Unstructured modeling is a rapidly developing field. This would be very useful in oceanography because of the nature of data collection in the WHOI ITP program. The use of an unstructured grid would allow the direct implementation of these modeling techniques without interpolation, thus, reducing one possible source of error.

In-situ measurements taken within several days would likely improve the model. We recommend that in-situ measurements need to be collected on a regularly spaced grid (similar to C-SALT experiment in Tropics). A clear snapshot of the Beaufort Sea at one specific time would significantly reduce error in the model. The dynamic nature of the Sea creates a source of error naturally. Modeling of this nature utilizes static forms of the equations and neglects any temporal variation. Thus, a timely set of in-situ measurements would likely improve the results.

THIS PAGE INTENTIONALLY LEFT BLANK

## LIST OF REFERENCES

- Caro, G. P. (2009), Direct numerical simulations of diffusive staircases in the Arctic. Master's thesis, Naval Postgraduate School, Monterey, CA.
- Dickson, R. R., Osborn T. J., Hurrell J. W., Meincke J., Blindheim J., Adlandsvic B., Vinje T., Alekseev G., & Maslowski W. (2000). The Arctic Ocean Response to the North Atlantic Oscillation. *Journal of Climate*, **13**, 2671-2696.
- Golub, G. H., Van Loan C. F. (1980). An analysis of the total least squares problem, *SIAM J. Numer. Anal.*, **17**, 883-893.
- Kelley, D. E. (1990). Fluxes through diffusive staircases: a new formulation, *J. Geophys. Res.*, **95**, 3365-3371.
- Kelley, D. E., Fernando H. J. S., Gargett A. E., Tanny J., & Ozsoy E. (2003). The diffusive regime of double-diffusive convection, *Progress in Oceanography*, **56**, 461-481.
- Krishfield, R., Toole J., Proshutinsky A., and Timmermans M.-L. (2008). Automated Ice-Tethered Profilers for seawater observations under pack ice in all seasons, *J. Atmos. Ocean. Tech.*, **25**, 2091-2105.
- Lee, J. H. (1991). The determination of velocities and diffusion coefficients from tracer distributions. PhD. Dissertation, Yale University, New Haven, CT.
- Lee, J. H., Veronis G. (1991). On the difference between tracer and geostrophic velocities obtained from C-SALT data, *Deep-Sea Res.*, **38**, 555-568.
- Markovsky, I., Van Huffel S. (2007), Overview of total least-squares methods, *Signal Processing*, **87**, 2283-2302.
- Marmorino, G. O., Caldwell D. R. (1976), Heat and salt transport through a diffusive thermohaline interface, *Deep-Sea Res.*, **23**, 59-67.

- Maslowski, W. and Clement-Kenney J. (2009), Influence of oceanic circulation, heat fluxes and eddies on recent warming in the western Arctic: results of a high-resolution ice-ocean model, *Unpublished White Paper*
- Merryfield, W. J. (2000), Origin of thermohaline staircases, *Journal of Physical Oceanography*, **30**, 1046-1068.
- Padman, L., Dillon T. M. (1987), Vertical heat fluxes through the Beaufort Sea thermohaline staircase. *Journal of Geophysical Research*, **108(C3)**, 1-21.
- Perovich, D. K., Grenfell T. C., Richter-Menge J. A., Light B., Tucker III W. B., and Eicken H. (2003), Thinner and thinner: Sea ice mass balance measurements during SHEBA, *Journal of Geophysical Research*, **108(C3)**, 8050, doi:10.1029/2001JC001079, 2003.
- Schmitt, R. W. (1994), Double diffusion in oceanography, *Annu. Rev. Fluid Mech.*, **26**, 255-285.
- Stroeve, J., and Maslowski W. (2008), Arctic Sea Ice Variability during the last Half Century, *Climate Variability and Extremes during the Past 100 Years*.
- Stroeve, J., Holland M. M., Meier W., Scambos T., and Serreze M. (2007), Arctic Sea Ice Decline: Faster than Forecast, *Geophysical Research Letters*, **34**, L09501, doi: 10.1029/2007GL029703.
- Timmermans, M.-L., Toole J., Krishfield R., and Winsor P. (2008), Ice-Tethered Profiler observations of the double-diffusive staircase in the Canada Basin thermocline, *J. Geophys. Res.*, **113**, C00A02, doi:10.1029/2008JC004829.
- Turner, J. S. (1973) *Buoyancy Effects in Fluids*. New York: Cambridge University Press.
- Turner, J. S., Veronis G. (2003), The Influence of Double-Diffusive processes on the melting of ice in the Arctic Ocean: laboratory analogue experiments and their interpretation, *Journal of Marine Systems*, **45**, 21-37
- Wilson, A. L. (2007), Structure and dynamics of the thermohaline staircases in the Beaufort Gyre. Master's thesis, Naval Postgraduate School, Monterey, CA.

- Yang, J. (2006), The Seasonal Variability of the Arctic Ocean Ekman Transport and its role in the Mixed Layer Heat and Salt Fluxes, *Journal of Climate*, **19**, 5366-5387.
- Zhang, J., Rothrock D. A., and Steele M. (1998), Warming of the Arctic Ocean by a strengthened Atlantic inflow: Model results, *Geophysical Research Letters*, **25**, 1745-1748.
- Zhang, J., Rothrock D. A., and Steele M. (2000), Recent Changes in Arctic Sea Ice: The interplay between Ice Dynamics and Thermodynamics, *Journal of Climate*, **13** 3099-3114.

THIS PAGE INTENTIONALLY LEFT BLANK

## INITIAL DISTRIBUTION LIST

1. Defense Technical Information Center  
Ft. Belvoir, Virginia
2. Dudley Knox Library  
Naval Postgraduate School  
Monterey, California
3. Professor Timour Radko  
Naval Postgraduate School  
Monterey, California
4. Professor Arthur Schoenstadt  
Naval Postgraduate School  
Monterey, California